Article

Microwave-Driven Hexagonal-to-Monoclinic Transition in BiPO$_4$: An In-Depth Experimental Investigation and First-Principles Study

Ana C. M. Tello, Marcelo Assis, Ricardo Menasce, Amanda F. Gouveia, Vinicius Teodoro, Natalia Jacomaci, Maria A. Zaghete, Juan Andrés, Gilmar E. Marques, Marcio D. Teodoro, Albérico B. F. da Silva, Jefferson Bettini, and Elson Longo*

Cite This: *Inorg. Chem.* 2020, 59, 7453−7468

Read Online

ACCESS | Metrics & More | Article Recommendations | SI Supporting Information

ABSTRACT: Present theoretical and experimental work provides an in-depth understanding of the morphological, structural, electronic, and optical properties of hexagonal and monoclinic polymorphs of bismuth phosphate (BiPO$_4$). Herein, we demonstrate how microwave irradiation induces the transformation of a hexagonal phase to a monoclinic phase in a short period of time and, thus, the photocatalytic performance of BiPO$_4$. To complement and rationalize the experimental results, first-principles calculations have been performed within the framework of density functional theory. This was aimed at obtaining the geometric, energetic, and structural parameters as well as vibrational frequencies; further, the electronic properties (band structure diagram and density of states) of the bulk and corresponding surfaces of both the hexagonal and monoclinic phases of BiPO$_4$ were also acquired. A detailed characterization of the low vibrational modes of both the hexagonal and monoclinic polymorphs is key to explaining the irreversible phase transformation from hexagonal to monoclinic. On the basis of the calculated values of the surface energies, a map of the available morphologies of both phases was obtained by using Wulff construction and compared to the observed scanning electron microscopy images. The BiPO$_4$ crystals obtained after 16−32 min of microwave irradiation provided excellent photodegradation of Rhodamine B under visible-light irradiation. This enhancement was found to be related to the surface energy and the types of clusters formed on the exposed surfaces of the morphology. These findings provide details of the hexagonal-to-monoclinic phase transition in BiPO$_4$ during microwave irradiation; further, the results will assist in the design of electronic devices with higher efficiency and reliability.
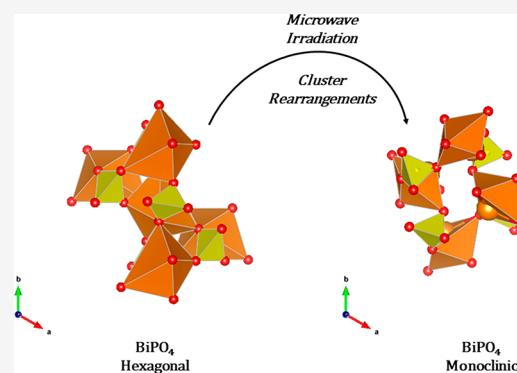
INTRODUCTION

Bismuth phosphate (BiPO$_4$) is a promising photocatalyst that is activated by visible light. It demonstrates double the activity of TiO$_2$ (P25, Degussa) for the degradation of organic dyes under ultraviolet (UV) light;[1] further, it exhibits enhanced photocatalytic activity toward NO purification.[2,3] BiPO$_4$ presents hexagonal and monoclinic polymorphs that comprise both distorted tetrahedral [PO$_4$] and octahedral [BiO$_6$] clusters, which are the primary building blocks of the polymorph. However, both polymorphs present different photocatalytic activities, which is highly dependent on the structure, electronic properties, and morphology of these phases; consequently, it is reliant on its exposed surfaces as well.[2,4−7] In particular, Fu et al.[8] have reported that the monoclinic phase of BiPO$_4$ is the preferred crystalline structure for the degradation of benzene; this is due to the structural distortion of the tetrahedral [PO$_4$] cluster and the large band gap structure.[9−11] The preparation of BiPO$_4$ polymorphs (hexagonal and monoclinic) has been successfully carried out by several methods. The pure hexagonal phase of BiPO$_4$ has already been obtained by conventional hydrothermal,[12]

microwave-assisted hydrothermal (MAH),[13] and sonochemical[14,15] methods under mild synthesis conditions. In turn, the pure monoclinic phase is usually obtained by the conventional hydrothermal method, which exhibits long synthesis periods (2−96 h) and temperatures of up to 200 °C.[1,2,16−18] Wang et al. also observed formation of the monoclinic phase using the MAH method but with the addition of an ionic liquid in the reaction medium.[19] Few studies in the literature also show conversion of the hexagonal phase to the monoclinic phase by the hydrothermal method[12] through the incorporation of compression[20] or doping processes.[21,22] Ding et al. observed complete conversion by employing the time frame of 1−3 h at a temperature of 200 °C.[23] Further, Zhu et al. required up to 12 h of synthesis at 150 °C to complete conversion of the
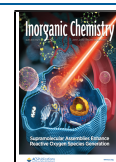
hexagonal phase to the monoclinic phase.[24] In these studies, it is evident that complete conversion from one phase to the other was directly proportional to the temperature employed during the synthesis.

Among the different solution-based synthesis techniques, microwave irradiation has garnered a widespread scope of remarkably new opportunities to explore its applications in the area of materials science. Microwave irradiation in a suitable solvent has been widely applied for the rapid synthesis of inorganic solids at relatively lower temperatures within a short reaction time (within minutes) compared to conventional heating;[25−27] further, it has received special attention owing to its interesting advantages, which include rapid, uniform, and selective heating, reduced processing costs, better production quality, and the possibility of modifying the phase stability and morphology beyond thermodynamic equilibrium. This has led to the fabrication of new materials that are technologically important such as metastable phases, which are not accessible by conventional methods.[28−30] Further, microwave heating is an inexpensive, facile, and relatively fast method for the preparation of crystalline samples, which exhibit unique or enhanced properties; these can be used to fabricate products with narrow particle size distribution and increased phase purity.[30−34] However, microwave-specific thermal and microwave nonthermal effects are still poorly understood, especially during synthesis procedures.[35]

Recently, the structures and energetics of four low-index stoichiometric surfaces [(001), (010), (011), and (100)] of monoclinic monazite $BiPO_4$ have been studied from a theoretical point of view by using density functional theory (DFT) calculations.[36] Fu et al.[37] showed that monoclinic $BiPO_4$ exhibits a dendritic morphology and performs as well as a photocatalyst for the degradation process of benzene; this is due to the presence of highly energetic (002), (012), and (031) surfaces and oxygen vacancies (V_O). However, the role of the exposed surfaces and morphology on the photocatalytic activity is still unrevealed. To the best of our knowledge, reports on the direct visualization of the transition process between hexagonal and monoclinic phases have been very limited; in addition, deep insight into the surface-dependent photocatalytic activity of both hexagonal and monoclinic polymorphs of materials based on $BiPO_4$ has not yet been carried out.

An attractive alternative, yet underexplored strategy to gain control over the phase transition is provided by regulating the microwave irradiation while keeping all other parameters constants. Therefore, understanding the phase transition process, at the atomic scale, can allow an efficient phase-controlled synthesis that leads to crystal structures with improved properties and thus may have new materials with the potential for various technological applications. Inspired by the above considerations, we report a novel study on the gradual transformation of hexagonal $BiPO_4$ to the monoclinic polymorph upon microwave irradiation without the addition of any surfactants and templates; the $BiPO_4$ microcrystals initially exhibit a hexagonal structure and are obtained by a simple coprecipitation (CP) method. Our principle aim was to understand the fine effects of microwave irradiation on the morphology and photoluminescence (PL) emissions of the as-synthesized $BiPO_4$ crystals and to investigate the role of the electronic structure on their photocatalytic activity. Herein, we elucidate these points by performing a detailed theoretical and experimental study on the photocatalytic activity in the

degradation process of Rhodamine B (RhB) under visible irradiation. The synthesized materials were characterized by X-ray diffraction (XRD) with Rietveld refinement, scanning electron microscopy (SEM), and micro-Raman spectroscopy. Moreover, their optical properties were investigated by using ultraviolet−visible (UV−vis) spectroscopy and PL measurements at room temperature. First-principles calculations within the framework of DFT were employed to obtain atomic-level information on the geometry and electronic structure, local bonding, band structure, density of states (DOS), and vibrational frequencies. The morphologies of the as-synthesized samples were obtained by SEM, and their corresponding transformations were rationalized; this was achieved by using the Wulff construction and altering the relative values of the surface energies of the different surfaces. The effect of time on the formation of hexagonal and monoclinic phases and on their structural, morphological, and absorption properties was investigated. Furthermore, by combining the results obtained from first-principles calculations and experimental measurements, the crystal structures, electronic properties, and surface energy characteristics of $BiPO_4$ were analyzed; this was aimed at achieving deep insight into their morphology characteristics, optical properties, and photocatalytic activities toward RhB. Accurate prediction of the structure, stability, electronic structure, and morphology of $BiPO_4$ is an essential prerequisite for tuning their electronic properties and functions.

This paper contains three more sections. The next section is the Experimental Section, where the synthesis, characterization, computational details, and model systems are elucidated. In section three, the results are presented and discussed. The main conclusions are summarized in the fourth section.

■ EXPERIMENTAL SECTION

Synthesis. The $BiPO_4$ samples were synthesized by the CP method at 30 °C in an aqueous medium. The precursors used were $Bi(NO_3)_3 \cdot 5H_2O$ (98%, Aldrich) and $(NH_4)_2HPO_4$ (98%, Alfa-Aesar). 1×10^{-3} mol of $Bi(NO_3)_3 \cdot 5H_2O$ and 1×10^{-3} mol of $(NH_4)_2HPO_4$ were dissolved separately in 30 mL of deionized water. The $Bi(NO_3)_3 \cdot 5H_2O$ solution was poured into the $(NH_4)_2HPO_4$ solution and stirred for 20 min. The suspensions obtained were transferred to a Teflon autoclave, sealed, and placed in the MAH system (2.45 GHz, maximum power of 800 W). The reaction mixtures were heated to 160 °C for 2, 4, 8, 16, and 32 min. Subsequently, the precipitate was decanted, washed several times with distilled water, and dried at 60 °C for 12 h.

Characterization. The $BiPO_4$ samples were structurally characterized by XRD using a D/Max-2500PC diffractometer (Rigaku) with Cu Kα radiation (λ = 1.5406 Å) in the 2θ range of 10−110° and a scanning speed of 1° min^{-1} in the Rietveld routine. The Rietveld refinement method was employed to understand the structural differences and phase composition of $BiPO_4$. In this analysis, the refined parameters were the scale factor, background, shift in the lattice constants, profile half-width parameters (u, v, and w), isotropic thermal parameters, lattice parameters, strain anisotropy factor, preferred orientation, and atomic functional positions. Further, micro-Raman spectra were recorded using the iHR550 spectrometer (Horiba Jobin-Yvon) coupled to a silicon charged-coupled-device (CCD) detector and an argon-ion laser (Melles Griot, Rochester NY), which was operated at 514.5 nm with a maximum power of 200 mW; moreover, a fiber-optic microscope was also employed. UV−vis diffuse-reflectance measurements were obtained using a Varian Cary spectrometer model 5G in the diffuse-reflectance mode, with a wavelength range of 200−800 nm and a scan speed of 600 nm min^{-1}. PL measurements were performed at room temperature by using a 355 nm laser (Cobolt/Zouk) as an excitation source, which was
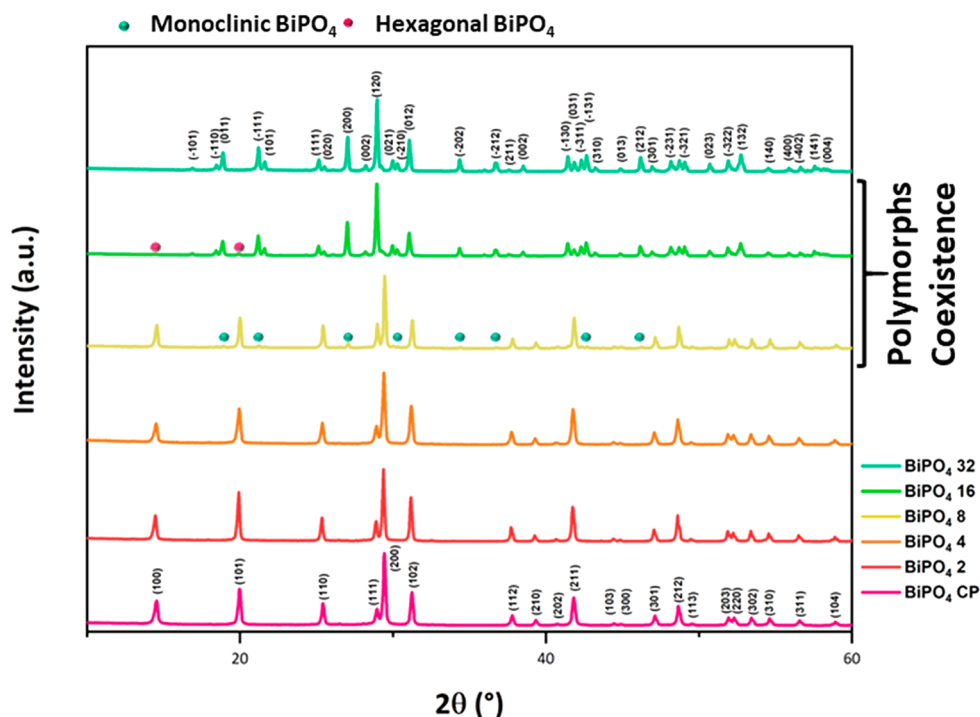
Figure 1. XRD patterns of $BiPO_4$ powders obtained by the CP method and under microwave irradiation at different times.

focused on a 200 μm spot at a constant power of 5 mW. The luminescence signal was dispersed by a 19.3 cm spectrometer (Andor/Kymera) and detected by a silicon CCD (Andor/IdusBU2). The morphologies, textures, and sizes of the samples were observed with a scanning electron microscope, which operated at 10 kV (Supra 35-VP, Carl Zeiss).

Photocatalysis. To perform the photocatalysis experiments, 50 mL of a RhB (95%, Mallinckrodt) solution (1×10^{-5} mol L^{-1}) was mixed with 50 mg of $BiPO_4$. The mixture, consisting of the dye and photocatalyst, was irradiated in a dark box using six lamps (Philips TL-D, 15 W). Before illumination, the suspensions were sonicated for 15 min in an ultrasonic bath (42 kHz, model 1510, Branson, MO) to allow saturated absorption of RhB onto the catalyst. Subsequently, the dispersion containing the catalyst and dye was transferred to a vessel inside the photoreactor, with the temperature maintained at 20 °C via a thermostatic bath and vigorous stirring in the dark for 30 min. After this process, the solution is exposed to light, and 2 mL aliquots were withdrawn at 0, 2, 4, 6, 8, 10, 15, 20, 30, 40, 50, and 60 min; each aliquot of the suspension was removed and placed in a centrifuge tube, which was then spun at 10000 rpm for 10 min to separate the solid catalyst from the liquid phase. Finally, the kinetics of the dye photodegradation process were monitored in a commercial cuvette via UV−vis spectroscopy (JASCO V-660) at 554 nm.

Computational Details and Model Systems. The hexagonal ($P3_121$) and monoclinic ($P121/n_1$) phases of $BiPO_4$ have been studied by using periodic DFT calculations with the B3LYP hybrid functional[38] using the *CRYSTAL14* code.[39] The Bi atom was described by using the effective core potential modified from Hay and Wadt,[40] while the P and O atoms were described from all-electron pob_TZVP_2012 basis sets,[41] as obtained from the CRYSTAL website.

The accuracy of the Coulomb and exchange integral calculations (TOLINTEG) was controlled by five parameters set to 10^{-7}, 10^{-7}, 10^{-7}, 10^{-7}, and 10^{-14}, and the reciprocal space was considered in a 6 × 6 mesh (SHRINK) corresponding to six independent k points in the Brillouin zone according to the Pack−Monkhorst method.[42] The band structure and DOS were obtained for 100 k points along the appropriate high-symmetry paths of the adequate Brillouin zone.

The equilibrium morphology of a crystal was calculated based on the classic Wulff construction,[43] by minimizing the total surface

energy (E_{surf}) at a fixed volume, providing a simple relationship between E_{surf} of the plane (hkl) and its distance in the normal direction from the center of the crystallite.[44] E_{surf} is defined as the energy per unit area required to form the surface relative to the bulk and calculated according to the equation

$$E_{surf} = \frac{E_{slab} - nE_{bulk}}{2A} \tag{1}$$

where E_{slab} is the energy of the relaxed slab, n is the number of $BiPO_4$ units in the slab, E_{bulk} is the energy of the bulk, and A is the surface area. The factor 2 in the denominator represents the upper and lower surfaces of the slab. The positions of all atoms of the slab were relaxed.

Slab models were employed to simulate the surfaces of low-index for both $BiPO_4$ hexagonal [with Miller indices (hkl): ($10\bar{1}0$), (0001), ($10\bar{1}1$), ($11\bar{2}0$), ($10\bar{1}2$), ($11\bar{2}2$), ($11\bar{2}1$)] and monoclinic [with Miller indices (hkl): (010), (100), (101), (011), ($1\bar{1}2$), (111), (001), ($1\bar{1}0$)] used in the calculations. The thickness of each slab model was optimized until convergence of the cutting energy was achieved. Calculations were carried out using slabs with atomic layers and periodic boundaries as the bulk in a and b directions, while c is a nonperiodic direction with a sufficient number of layers to minimize the interaction between the upper and lower surfaces of the slab. The number of layers in the slabs for the hexagonal phase is 51 for ($10\bar{1}0$), 36 for (0001), 54 for ($10\bar{1}1$), 50 for ($11\bar{2}0$), 80 for ($10\bar{1}2$), 90 for ($11\bar{2}1$), and 106 for ($11\bar{2}2$), and the thickness values corresponding to the number of layers to each surface are 1.796, 1.856, 1.615, 1.746, 1.409, 1.433, and 1.540 nm, respectively. The number of layers in the slab for the monoclinic phase was selected as 72 for the (100), (011), ($1\bar{1}2$), (111), (001), and ($1\bar{1}0$) surfaces and 60 for the (010) and (101) surfaces, and the thickness values corresponding to the number of layers to each surface are 1.748, 1.937, 1.713, 1.950, 1.467, 1.400, 1.905, and 1.885 nm, respectively. Furthermore, in order to reduce the calculation cost and keep charge neutrality, the stoichiometry of the slab model is maintained as that in the bulk model.

The procedure to obtain the complete set of morphologies, which are based on the Wulff construction and surface energy, was previously presented by our research group;[45] further, it was successfully used to obtain the morphology of materials, including

$PbMoO_4$, α-Ag_2MoO_4, $BaMoO_4$, $BaWO_4$, $CaWO_4$, Ag_3PO_4, Ag_2CrO_4, and $LaVO_4$.[46−53]

In addition, the broken bonding density (D_b), which is defined as the number of bonds broken per unit cell area when a surface is created, can be calculated by the equation[54,55]

$$D_b = \frac{N_b}{A} \quad (2)$$

where N_b is the number of broken bonds per unit cell area on a specific surface and A is the area unit of the surface. From the values derived from D_b, we can predict the order of the surface stability because we know that higher values are related to larger quantities of defects present on the surface.[56]

The polyhedron energy (E_{poly}) was calculated with eq 3, and energy profiles were constructed, allowing us to associate the ideal morphology with the final experimental morphology.

$$E_{poly} = \sum C_i E_{surf}^{(hkl)} \quad (3)$$

where C_i is the percentage contribution of the surface area to the total area of the polyhedron ($C_i = A^{(hkl)}/A^{poly}$) and $E_{surf}^{(hkl)}$ is the surface energy.[57]

■ RESULTS AND DISCUSSION

XRD. Figure 1 shows the XRD patterns of the $BiPO_4$ samples obtained by the CP method and also of those subjected to microwave irradiation at different times. XRD analysis were performed to demonstrate the order/disorder transition at long-range or to determine the periodicity and arrangement of the crystalline lattice. All samples exhibit well-defined diffraction peaks, indicating a good degree of structural order at long-range in the crystalline lattice.

The samples synthesized by the CP method and irradiated by microwave at 2 and 4 min correspond to $BiPO_4$ with hexagonal structure and space group $P3_121$; this was in accordance with card no. 67986[58] in the Inorganic Crystal Structure Database (ICSD) with lattice parameters $a = 6.9885$ Å, $c = 6.4867$ Å, $\alpha = \beta = 90°$, and $\gamma = 120°$. For the samples irradiated by microwave at 8 and 16 min, formation of the monoclinic phase of $BiPO_4$, belonging to the space group $P121n/1$, was observed in addition to that of the hexagonal phase of $BiPO_4$; this was in accordance with card no. 67987[58] in the ICSD. The lattice parameters of the monoclinic phase are $a = 6.7626$ Å, $b = 6.9516$ Å, $c = 6.4822$ Å, $\alpha = \gamma = 90°$, and $\beta = 103.7°$. For the sample obtained after 32 min, only the monoclinic phase was observed. Thus, by increasing the time of exposure of microwave irradiation, complete conversion occurs from the hexagonal phase to the monoclinic phase. A schematic 3D representation of the hexagonal and monoclinic structures of $BiPO_4$ is depicted in Figure 2, and theoretical and experimental values of the P−O and Bi−O distances and O−P−O and O−Bi−O angles are presented in Tables SI-1 and SI-2.

The parameters obtained in the Rietveld refinements of $BiPO_4$ powders are shown in Tables SI-3 and SI-4, and their structural results are presented in Figure 3, in which the statistical fitting parameters (R_{wp} and goodness of fit; Table SI-3) indicate that the quality of structural refinement data is acceptable (Figure SI-1). The calculated equilibrium lattice parameters of the two phases of $BiPO_4$ are also shown in Table SI-4.

An analysis of the results presented in Tables SI-1 and SI-2 renders slight differences between the calculated and experimental data of bond distances and angles, which can be attributed to differing synthesis conditions. Following the
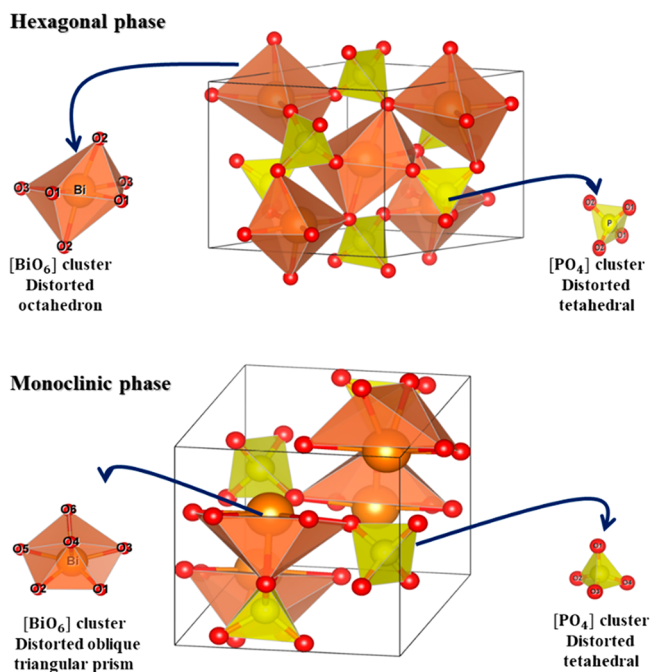

Figure 2. 3D representation of the hexagonal and monoclinic $BiPO_4$ structures. The $[BiO_6]$ and $[PO_4]$ clusters, as building blocks of these materials, are displayed.

proposals of Xu et al.[36] and Zhu et al.,[59] we assumed that both polymorphs can be described by $[BiO_6]$ and $[PO_4]$ clusters.

Thus, more specifically, the $[BiO_6]$ clusters correspond to a distorted octahedron in the hexagonal phase with the Bi−O bond length in the range of 2.368−2.558 Å (Table SI-3) and a distorted oblique triangular prism in the monoclinic phase with the bond length of Bi−O in the range of 2.326−2.523 Å (Table SI-4). Both the $[BiO_6]$ and $[PO_4]$ clusters are more distorted in the monoclinic polymorph with respect to the hexagonal one. The larger variety of Bi−O and P−O bonds in monoclinic $BiPO_4$ is responsible for the significant structural distortions at both the $[BiO_6]$ and $[PO_4]$ clusters. Such behavior is primarily observed in the $[PO_4]$ tetrahedron and has been assumed to be responsible for the higher photocatalytic activity of the monoclinic polymorph compared to the hexagonal phase of $BiPO_4$.[60,61]

It is observed in Figure SI-2A that a partial conversion between the hexagonal and monoclinic phases occurs after 8 min of microwave irradiation, while a pure monoclinic polymorph is obtained at 32 min. In order to understand how the conversion between phases occurs, an analysis of the lattice parameters was performed from the Rietveld refinement data. It is observed that, during the first 4 min of microwave irradiation, there is a reduction in the a and c lattice parameters of the hexagonal structure; this indicates a contraction of the crystalline cell (Figure SI-2B,C). The phase transformation process from hexagonal to monoclinic requires energy, which was supplied by dipolar polarization of the water solvent and ionic conduction from the dissolved precursors in the reaction medium; this led to rapid heating of the system, which enhanced the energy-transfer process during microwave irradiation.[62] The energy provided to the system is used to induce a rearrangement in the positions of atoms in the unit cell; i.e., the Bi and P cations in the $[BiO_6]$ and $[PO_4]$ clusters, respectively, undergo changes in both the Bi−O and P−O bond lengths as well as the O−Bi−O and O−P−O bond
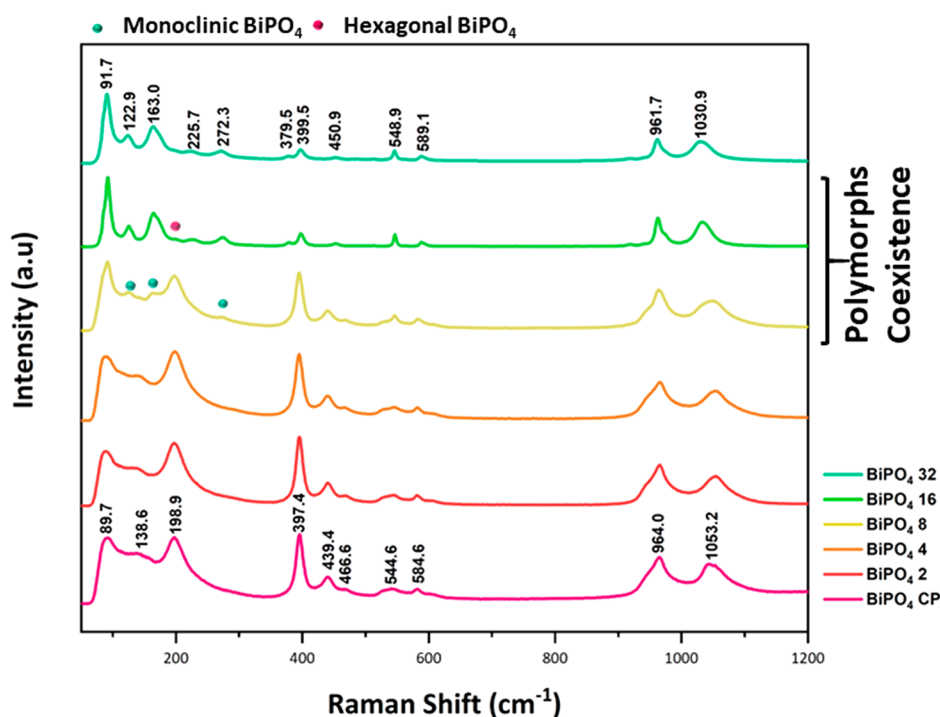
Figure 3. Micro-Raman spectra of $BiPO_4$ powders obtained by the CP method and under microwave irradiation at different times.

angles. The sample obtained after 4 min of microwave irradiation has sufficient energy to induce structural distortions at these clusters, which are essentially precursors of the monoclinic structure. After 8 min of microwave irradiation, an expansion in the lattice parameters of the hexagonal phase was observed, until it was completely converted into a monoclinic polymorph. When the monoclinic phase is formed, the hexagonal unit cell relaxes and expansion of the crystal lattice can be detected. Otherwise, when both phases coexist, a decrease in the values of the lattice parameters (a, b, and c) can be observed (Figure SI-2D−F) for the monoclinic phase. However, when the monoclinic phase is obtained, there is an increase in the values of these lattice parameters.

Micro-Raman Spectroscopy. Micro-Raman spectroscopy (Figure 3) is an important technique for understanding the effects of structural order/disorder transition at short-range in crystalline solids. The Raman spectrum for a crystal without defects should be comprised of lines corresponding with central points in the allowed zone, which is in accordance with the rules of selection. According to group theory analysis, the allowed representation for each of the corresponding Wyckoff positions of the hexagonal structure of $BiPO_4$ in the symmetry group D_3^4 indicates 26 active Raman modes corresponding to decomposition at the point $\Gamma = (8A_1 + 18E_1)$.[10] For the monoclinic structure of $BiPO_4$, which belongs to the symmetry group C_{2h}^4, 36 corresponding Raman active modes of decomposition of the point $\Gamma = (18A_g + 18 B_g)$ are obtained.[10,63] Micro-Raman spectra of the samples synthesized in 4 min exhibit only active modes that are associated with the hexagonal phase; for samples synthesized in 8 min, the appearance of the active modes of the monoclinic phase can be observed. For the sample synthesized after 32 min, only the modes referring to the monoclinic structure were observed in Raman as well as XRD spectra; this indicates complete conversion of the hexagonal structure to a monoclinic one.

For the hexagonal structure of $BiPO_4$, 11 modes are observed. There are three modes located at 89.7, 138.6, and 198.9 cm^{-1}, which are assigned to the symmetric bending of the O−Bi−O moiety.[10,13,14,64] The three modes observed at 397.4, 439.4, and 466.6 cm^{-1} are related to the bending vibrations (ν_2) of the $[PO_4]$ clusters.[10,13,14,64] The Raman modes observed at 544.6 and 584.6 cm^{-1} are attributed to the asymmetric stretching vibrations (ν_4) of the $[PO_4]$ cluster.[10,13,14,64] The most intense modes, observed at 964.0 and 1053.2 cm^{-1}, are associated with symmetric stretching vibrations (ν_1).[10,13,14,64] For the monoclinic structure of $BiPO_4$, 13 modes are observed. The modes located at 91.7, 122.9, 163.0, 225.7, and 272.3 cm^{-1} are associated with stretching of the Bi−O bonds.[6,65] The modes observed at 379.5 and 399.5 cm^{-1} correspond to the bending vibrations (ν_2) of the $[PO_4]$ clusters, while the modes at 450.9, 548.9, and 589.1 cm^{-1} correspond to the bending vibrations (ν_4) of the $[PO_4]$ clusters.[6,65] The highest-intensity modes at 961.7 and 1030.9 cm^{-1} are related to the symmetric (ν_1) and asymmetric (ν_3) stretching modes of the cluster $[PO_4]$, respectively.[6,65] Further, it was observed that samples that are subjected to synthesis for up to 4 min comprise only the modes that are associated with the hexagonal phase; meanwhile, for synthesis above 8 min, the samples display active modes for the monoclinic phase. For the sample synthesized with 32 min, as well as in the XRD spectrum, only the modes associated with the monoclinic structure are observed; this indicates a complete conversion of the hexagonal structure to a monoclinic one.
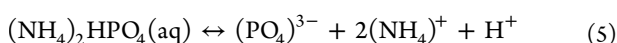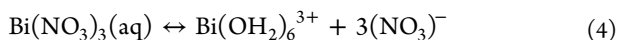
Figure SI-3 displays a comparison between the experimental and calculated values of the Raman modes of both the hexagonal (Figure SI-3A) and monoclinic (Figure SI-3B) structures. Both the experimental and theoretical results are in accordance with the results previously reported in the literature (Tables SI-5 and SI-6),[10] which indicates that our computa-

tional methodology and optimized unit cells provide a good representation of the two polymorphs of $BiPO_4$.

Proposed Mechanism. On the basis of analysis of the above results and, in particular, the characteristics of both the $[BiO_6]$ and $[PO_4]$ clusters along the transformation from hexagonal to monoclinic structure, we propose the following mechanism for the formation of both polymorphs and their subsequent irradiation transformation.

$Bi(NO_3)_3(aq)$ and $(NH_4)_2NaPO_4(aq)$ are the precursors of the Bi and P cations, respectively, along the CP synthesis method, and their environments control the geometry and electronic properties of both the $[BiO_6]$ and $[PO_4]$ clusters, as final constituents of both the hexagonal and monoclinic polymorphs of $BiPO_4$.

First, $Bi(NO_3)_3$ was dissolved in water, giving the hexahydrate complex of eq 4, while the phosphate source was dissolved in water to form $(PO_4)^{3-}$ (eq 5); both processes can be described as a chemical equilibrium.

$$Bi(NO_3)_3(aq) \leftrightarrow Bi(OH_2)_6^{3+} + 3(NO_3)^- \qquad (4)$$

$$(NH_4)_2HPO_4(aq) \leftrightarrow (PO_4)^{3-} + 2(NH_4)^+ + H^+ \qquad (5)$$

On the other hand, $(Bi(OH_2)_6)^{3+}$ and $(PO_4)^{3-}$ can be considered to be precursors of the $[BiO_6]$ and $[PO_4]$ clusters in the solid state, respectively. In the next step, both clusters are capable of forming the hexagonal $BiPO_4$ phase, and posterior microwave irradiation converts this to the monoclinic $BiPO_4$ polymorph, as is represented in Figure SI-4.

Along the CP method used to obtain $BiPO_4$, formation of the hexagonal polymorph, with the presence of $[BiO_6]$ and $[PO_4]$ clusters with minor structural distortions, is favored because of the low temperature and mild conditions. When this polymorph is irradiated by microwaves, a combination of recrystallization/dissolution processes are promoted and a symmetrical breaking process takes place, in which more structurally distorted $[BiO_6]$ and $[PO_4]$ clusters appear, enhancing formation of the monoclinic polymorph. As reported in the literature, the phase transition requires only a small rotation of the polyhedron for a suitable symmetrical arrangement;[38,40,66] therefore, it is expected that coherent coupling between the microwave field radiation with low-frequency modes of the system, translational and rotational modes, can induce structural changes at both the $[BiO_6]$ and $[PO_4]$ clusters.

The theoretical vibrational spectrum presents five low-frequency modes (<100 cm^{-1}) in hexagonal $BiPO_4$ at wavelengths of 66.57, 70.68, 77.7, 85.6, and 97.45 cm^{-1}. By analysis of the animation of these vibrational modes using *CRYSPLOT*, we can visualize the atomic movements in each wavelength. The phase transition of hexagonal to monoclinic is then attributed to a combination of these five modes; i.e., the mode at 66.57 cm^{-1} is responsible of displacement of the Bi cation, the vibrational mode at 70.67 cm^{-1} (Figure 4) is linked to rotation of the O anions at the $[BiO_6]$ cluster, and the vibrational mode at 77.7 cm^{-1} is assigned to rotation of the O anions at the $[PO_4]$ cluster.

These findings seem to indicate that the energetic stimuli provided by microwave irradiation are capable of activating these low vibrational modes to enhance the phase transformation from the hexagonal polymorph to the monoclinic polymorph. At local coordination, the distorted octahedron $[BiO_6]$, at the hexagonal phase, undergoes a structural rearrangement to the distorted oblique triangular prism
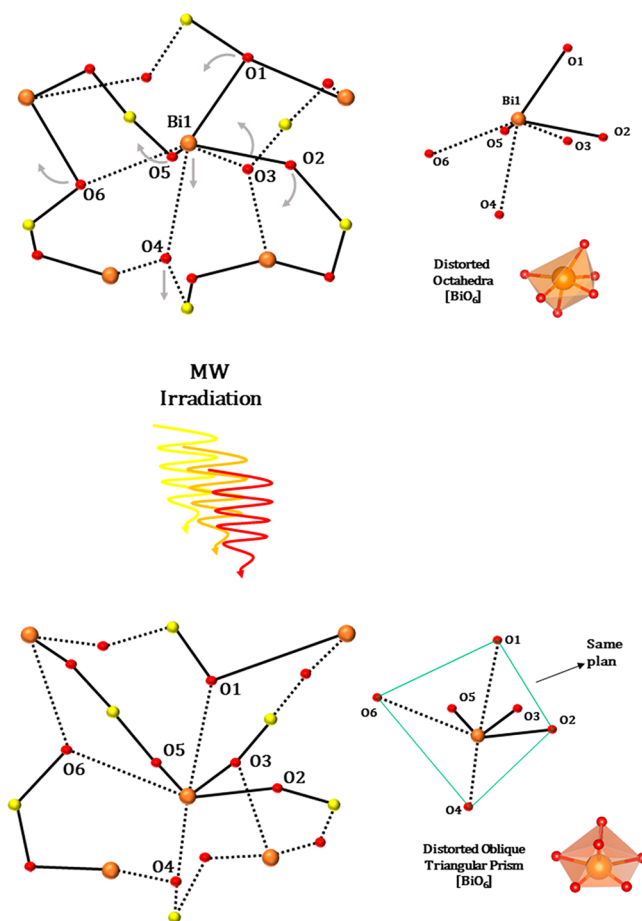

Figure 4. Representation of the vibration mode located at 70.67 cm^{-1}, associated with rotation of the O anions at $[BiO_6]$ that are responsible for the phase transition from the hexagonal (distorted octahedra $[BiO_6]$) to monoclinic (distorted oblique triangular prism $[BiO_6]$) polymorph of $BiPO_4$ under microwave irradiation.

$[BiO_6]$ in the monoclinic polymorph. This monoclinic $BiPO_4$ phase presents low vibrational modes at 71.3 and 78.28 cm^{-1}, but the corresponding movements are not associated with transformation from the monoclinic to hexagonal polymorph. Therefore, these results seem to indicate that the phase transition from hexagonal to monoclinic, induced by microwave irradiation, corresponds to an irreversible process.

A note of caution is mandatory here; our previous analysis is based on the low vibrational modes of the hexagonal phase to explain the initial vibrational modes responsible for the phase transition, but a correct explanation needs to be obtained by characterizing the transition state, and, in particular, their transition vector, i.e., their unique imaginary vibration mode that controls this phase transition.

PL Emissions. PL measurements were also performed in order to investigate the influence of the structural ordering of defects of the $BiPO_4$ samples. Figure 5A shows the PL emissions under UV-laser excitation ($\lambda = 355$ nm). All samples show PL emission in the range of the visible spectrum with a broad-band profile, which is characteristic of multiphonon processes, ruled out by the presence of a high density of electronic levels within the band gap.[67−70] In order to verify the whole PL emission, an analysis by the Commission Internationale de L'Éclairage (CIE) coordinates was performed by *SpectraLux* software.[71] Figure 5B shows the CIE
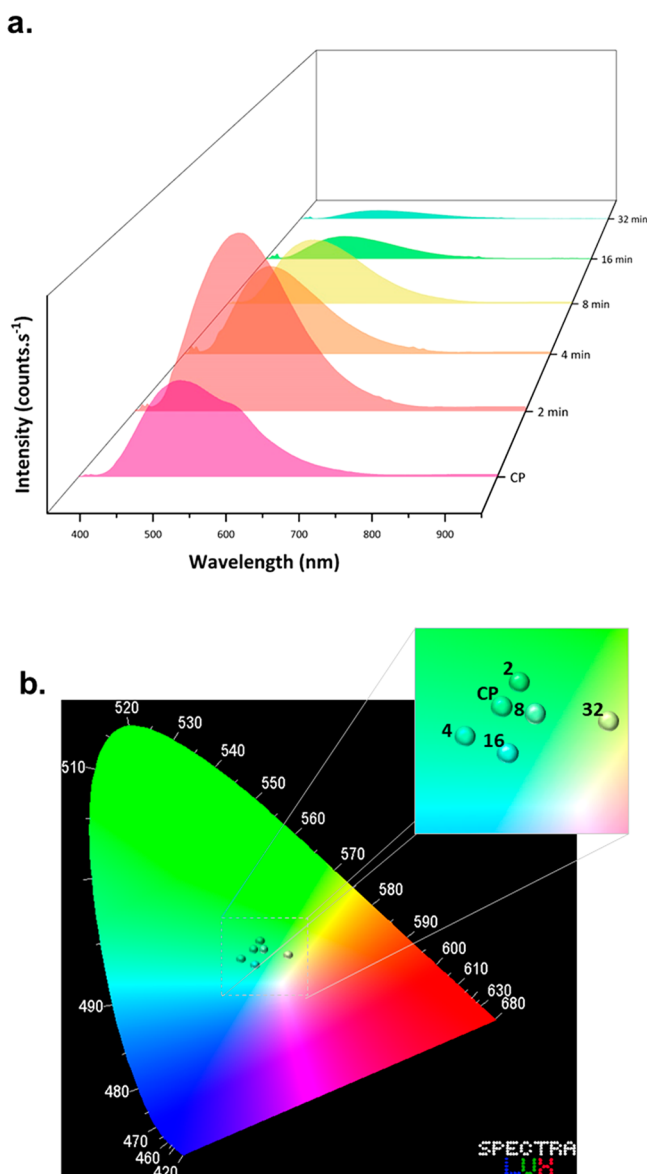
a.

b.

Figure 5. (a) PL spectra of BiPO$_4$ powders obtained by the CP method and posterior microwave irradiation at different times. (b) CIE chromaticity coordinates for the samples obtained by *SpectraLux* software.

chromaticity diagram for the PL spectra of all samples. Although there are slight differences in the color shades, all samples presented emissions in the green region of the visible spectrum.

The PL emissions were deconvoluted using the Voigt function, to quantify the contributions of each defect to the PL emission, as shown in Figure SI-5. There were three components centered at 470, 535, and 607 nm, corresponding to blue, green, and orange of the visible spectrum, respectively. It is known that each emitted color derives from an associated type of defect acting as a luminescent center within the material.[72−74] In the broad-band PL model, defects that emit higher energy in the visible spectrum, such as blue and violet, are assigned to structural defects, i.e., angular distortions at the [BiO$_6$] and [PO$_4$] clusters, which leads to larger changes in the electronic levels of the material, termed shallow defects. The emission of green and orange is associated with the presence of V$_O$, presenting a range of energies due to the contribution of

charge transfer between neutral (V$_O^x$), monoionized (V$_O^\bullet$), and doubly ionized (V$_O^{\bullet\bullet}$) states of oxygen vacancies, also called deep defects.[75−77]

Table SI-7 presents the contribution of the components of the PL spectra. We observed that the blue contribution, which corresponds to structural defects raised in the initial 4 min of synthesis, decreased as a function of the time of exposure of microwave irradiation. The sample obtained at 4 min of microwave irradiation presents higher structural distortions compared to other samples studied by Rietveld refinement, and a larger contraction of both the *a* and *c* lattice parameters can be sensed. These structural strains induce angular distortions on the clusters that compose the unit cell. To gain deeper insight into the nature of the structural and electron changes, the green and orange components in the emission (corresponding to the presence of V$_O$) were summed and considered to be deep defects in Table SI-7. Analysis of the results indicates that while blue coloration increases, the deep defect contribution decreases. It is believed that V$_O$ originate from variations in the Bi/P−O bond lengths and that this is a sign of an increase in the structural distortions at both the [BiO$_6$] and [PO$_4$] clusters and, subsequently, growth in the lattice parameters of the unit cell. It can also be noted that the 8 min sample shows expansion of both the *a* and *c* lattice parameters of the unit cell; we also see an increase in the contribution of deep defects to the PL emissions. In the 16 min sample, a slight increase in the blue contribution is observed in comparison to the 8 min sample, indicating a decrease in deep defects. These changes can also be confirmed by the results of Rietveld refinement due to a slight decrease of the lattice parameter *c* of the hexagonal unit cell. This contraction arises possibly because of the abrupt increase in the monoclinic phase content compared to that of the 8 min sample, which can generate a mismatch in the interface between both phases. These results indicate that the strain in the lattice parameter *c* axis had a large contribution to the defects that act as luminescent centers for the BiPO$_4$ samples. The sample irradiated for 32 min presents an increase in the deep contribution versus 16 min, which can also be confirmed by enlargement of the *a*, *b*, and *c* lattice parameters of the monoclinic unit cell. This behavior can be considered to be a signature of the presence of both V$_O$ and distorted [BiO$_6$] and [PO$_4$] clusters. Therefore, we are capable of connecting the results of the PL emissions and Rietveld refinement; i.e., larger structural distortions involving the Bi−O and P−O distances and O−Bi−O and O−P−O bond angles increase the contribution to the blue emission. Moreover, with an increase of V$_O$, a larger expansion of the unit cell takes place with a concomitant increase of the green and orange emissions.

Electronic Properties of the Bulk. The band structures were obtained for 100 *k* points along the appropriate high-symmetry paths of the adequate Brillouin zone, and the DOS were calculated for analysis of the corresponding electronic structures. Figures SI-6 and SI-7 present the band structure, the total DOS projected in all atoms of the bulk and surfaces for both polymorphisms, and also the partial DOS (PDOS) projected in the s and p (p$_x$, p$_y$, and p$_z$) orbitals in the bulk for the two BiPO$_4$ structures. As can be observed in Figure SI-6, for the BiPO$_4$ hexagonal phase, the top of the valence band (VB) is located between the K and H points of the Brillouin zone and the bottom of the conduction band (CB) is also located at the same region of the *k* space close to the H point. The calculated band gap value is 5.40 eV, corresponding to an

indirect transition, while the experimental value in this work is 4.60 eV.

In the case of the monoclinic phase (Figure SI-7), the top of the VB is located mainly between the D and C points and the bottom of the CB is located at the region between the E and Γ points. The band gap calculated is 4.60 eV, corresponding to an indirect transition, and the experimental value reported in this work is 3.80 eV. Band gap experimental values between 3.5 and 4.6 eV have been reported that depend on the size of the particle and the method of synthesis.[59,66,78]

On the basis of analyses of DOS and PDOS, it can be deduced that, for both hexagonal and monoclinic BiPO$_4$, the VB is predominantly formed by the contribution of O atoms, with a small contribution of P and Bi atoms. In this VB, an overlap of the O 2p$_z$ orbitals with the Bi 6s orbitals occurs. The CB is formed mainly by the 6p$_z$ orbitals from the Bi atoms, with a small contribution of the 2p$_z$ orbitals of the O atoms and the 2p orbitals of the P atoms. These results are in accordance with other calculations reported in the literature.[59,66,78]

SEM Analysis. The SEM images of the morphologies of the obtained BiPO$_4$ samples are displayed in Figure 6.
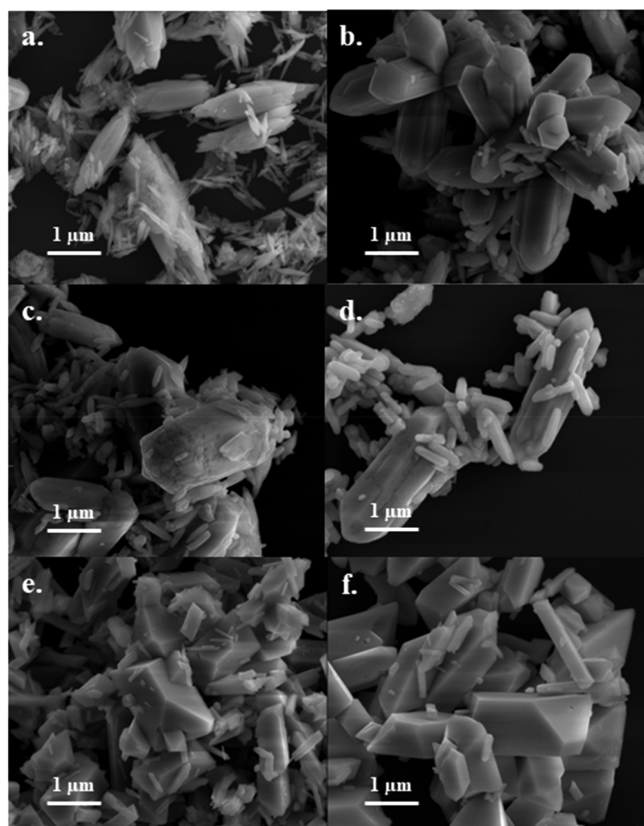

Figure 6. SEM images of BiPO$_4$ powders obtained by (**a**) the CP method and at (**b**) 2, (**c**) 4, (**d**) 8, (**e**) 16, and (**f**) 32 min of microwave irradiation.

It is clearly seen that the synthesized BiPO$_4$ suffers a change in its shape with an increase of the microwave irradiation. The BiPO$_4$ obtained by the CP method (hexagonal phase) has the shape of needles that agglomerate to form larger deformed rods (Figure 6A). When BiPO$_4$ is subjected to microwave irradiation at 2, 4, and 8 min (Figure 6B−D), the hexagonal phase is predominantly observed, and there is an increase in

the size of the needles that form the rod microstructure, and well-defined hexagonal rods appear. When the monoclinic phase is predominant, at 16 and 32 min of microwave irradiation (Figure 6E,F), the microstructures change into beveled tetragonal rods. This effect is due to the continuous dissolution/recrystallization processes that occur in BiPO$_4$ induced by microwave irradiation, and thus structural changes take place at short, medium, and long distances, as discussed above.

Structure of the BiPO$_4$ Surfaces. The key to investigating photocatalysis on the model surfaces is a detailed knowledge of the bare surface structures. In the absence of this information, mechanistic interpretation of the photochemical reactions can only be speculative. Sometimes, it may simply be incorrect. Through direct tracking, the evolution of the crystal surfaces using a combination of SEM images and first-principles calculations on the model BiPO$_4$ surfaces for both hexagonal and monoclinic polymorphs is discussed. Then the details of our photocatalysis on the model surfaces are presented, attempting to probe the Bi−O and/or P−O bond cleavage(s) with the formation of undercoordinated [BiO$_6$] and [PO$_4$] clusters at the exposed surfaces step by step. Figure 7 displays the slab models of the $(11\bar{2}1)$, (0001), $(11\bar{2}2)$, $(11\bar{2}0)$, $(10\bar{1}2)$, $(10\bar{1}1)$, and $(10\bar{1}0)$ surfaces of the hexagonal BiPO$_4$, while in Figure 8, the slab models of the $(1\bar{1}0)$, (010), $(1\bar{1}2)$, (011), (111), (100), (101), and (001) surfaces for the monoclinic BiPO$_4$. At the top of each surface model, Figures 7 and 8 show different kinds of undercoordinated clusters for the Bi and P cations compared to the bulk, which are generated because of direct cutting of the crystal along the surface in the slab construction where different bonds have been broken.

Thus, for the hexagonal phase, the $(10\bar{1}0)$ and (0001) surfaces present only one kind of undercoordinated cluster, $[\text{BiO}_5 \cdot V_O^x]$, and it is worth noting that all studied surfaces present this kind of undercoordinated cluster, with the exception of the $(10\bar{1}1)$ surface, which presents only an undercoordinated cluster, $[\text{PO}_3 \cdot V_O^x]$. On the $(11\bar{2}0)$ surface, the undercoordinated clusters of $[\text{BiO}_5 \cdot V_O^x]$ and $[\text{BiO}_4 \cdot 2V_O^x]$ are present. The $(10\bar{1}2)$ surface is formed by $[\text{BiO}_5 \cdot V_O^x]$, $[\text{BiO}_4 \cdot 2V_O^x]$, and $[\text{PO}_3 \cdot V_O^x]$ clusters. The most unstable surfaces, $(11\bar{2}1)$ and $(11\bar{2}2)$, are formed by the undercoordinated $[\text{BiO}_5 \cdot V_O^x]$ and $[\text{PO}_2 \cdot 2V_O^x]$ clusters, which are common to both surfaces, while on the $(11\bar{2}2)$ surface, the $[\text{BiO}_3 \cdot 3V_O^x]$ clusters appear, and on the $(11\bar{2}1)$ surface, the $[\text{BiO}_4 \cdot 2V_O^x]$ and $[\text{PO}_3 \cdot V_O^x]$ clusters are found.

In the case of the monoclinic phase, the undercoordinated Bi cation and $[\text{BiO}_5 \cdot V_O^x]$, $[\text{BiO}_4 \cdot 2V_O^x]$, and $[\text{BiO}_3 \cdot 3V_O^x]$ clusters can be observed and the undercoordinated $[\text{PO}_3 \cdot V_O^x]$ and $[\text{PO}_2 \cdot 2V_O^x]$ clusters centered around the P cation can be sensed. More specifically, the (010), (100), (101), and (011) surfaces are characterized for only the undercoordinated $[\text{BiO}_5 \cdot V_O^x]$ cluster. In the case of the $(1\bar{1}2)$ surface, the $[\text{BiO}_4 \cdot 2V_O^x]$, $[\text{BiO}_3 \cdot 3V_O^x]$, and $[\text{PO}_3 \cdot V_O^x]$ clusters can be observed. On the other hand, the (111) surface presents four kinds of undercoordinated clusters: $[\text{BiO}_5 \cdot V_O^x]$, $[\text{BiO}_4 \cdot 2V_O^x]$, $[\text{BiO}_3 \cdot 3V_O^x]$, and $[\text{PO}_3 \cdot V_O^x]$. The (001) surface displays the $[\text{BiO}_4 \cdot 2V_O^x]$ and $[\text{PO}_3 \cdot V_O^x]$ clusters, while the $(1\bar{1}0)$ surface is formed for the undercoordinated $[\text{BiO}_5 \cdot V_O^x]$ and $[\text{BiO}_4 \cdot 2V_O^x]$ clusters, and it is the only surface that presents $[\text{PO}_2 \cdot 2V_O^x]$ clusters.

By a comparison of the calculated E_{surf} values shown in Tables SI-8 and SI-9, it is possible to establish an order of the thermodynamic stability for these surfaces; thus, for the BiPO$_4$
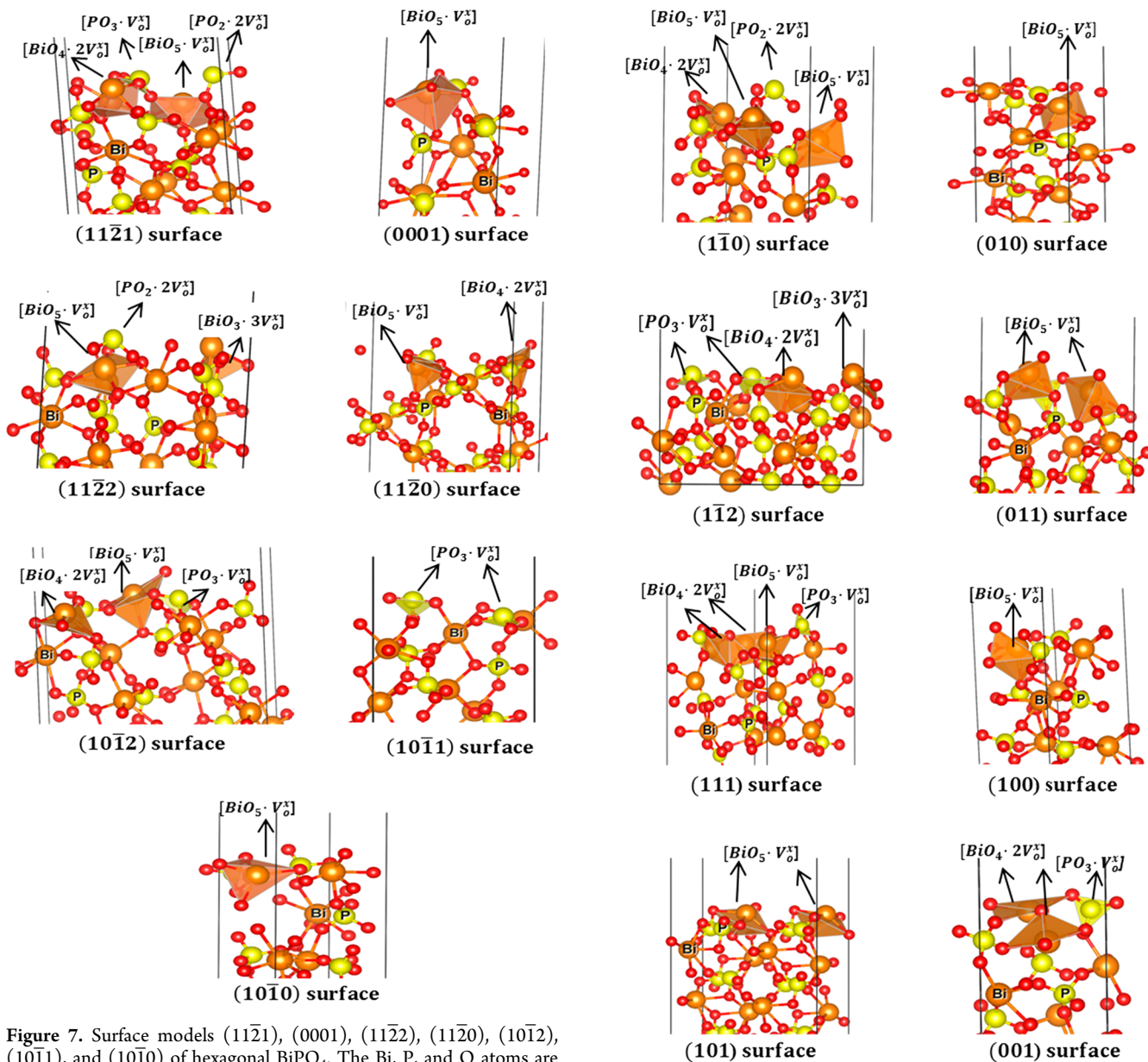
Figure 7. Surface models $(11\bar{2}1)$, (0001), $(11\bar{2}2)$, $(11\bar{2}0)$, $(10\bar{1}2)$, $(10\bar{1}1)$, and $(10\bar{1}0)$ of hexagonal $BiPO_4$. The Bi, P, and O atoms are represented by orange, yellow, and red balls, respectively. The undercoordination clusters for Bi and P atoms present at the top of each surface are also displayed. The V_O are indicated using the Kröger–Vink notation.

Figure 8. Surface models $(1\bar{1}0)$, (010), $(1\bar{1}2)$, (011), (111), (100), (101) and (001) of monoclinic $BiPO_4$. The Bi, P, and O atoms are represented by orange, yellow, and red balls, respectively. The undercoordination clusters for Bi and P atoms present at the top of each surface are also displayed. The V_O are indicated using the Kröger–Vink notation.

hexagonal, the order of decreasing stability is established as $(10\bar{1}0) > (0001) > (10\bar{1}1) > (11\bar{2}0) > (10\bar{1}2) > (11\bar{2}1) > (11\bar{2}2)$, while for the $BiPO_4$ monoclinic, the order of decreasing stability is $(010) > (100) > (101) > (011) > (1\bar{1}2) > (111) > (001) > (1\bar{1}0)$.

With the E_{surf} values reported in Tables SI-8 and SI-9 and employing the Wulff construction method, the ideal crystal morphology for each polymorph, as well as the complete map of available morphologies by changing the E_{surf} values (increases or decreases) of the different surfaces, was constructed. Figures 9 and 10 (top) show the available morphologies of both the hexagonal and monoclinic polymorphs of $BiPO_4$. Experimental SEM images are also included for comparison purposes with the calculated morphologies.

The ideal morphology of the hexagonal phase is characterized by a 6-fold geometry (Figure 9) that is controlled by the $(10\bar{1}0)$, (0001), and $(10\bar{1}1)$ surfaces. Starting from the ideal morphology and aimed at obtaining a morphology similar to the experimental SEM images, which present a 6-fold pyramidal geometry, the values of the surface energy for $(10\bar{1}0)$ and $(10\bar{1}1)$ were decreased and the surface energy for (0001) was increased simultaneously. On the other hand, a similar morphology of the experimental geometry can also be obtained through stabilization of the $(10\bar{1}2)$ surface. However, we associated the experimental morphology with the controlled morphology for the $(10\bar{1}1)$ surface, as reported by Li et al.,[13] in which the high-resolution transmission electron

Figure 9. Available morphologies of hexagonal $BiPO_4$ obtained by the Wulff construction considering the $(10\bar{1}0)$, (0001), $(10\bar{1}1)$, $(11\bar{2}0)$, $(10\bar{1}2)$, $(11\bar{2}2)$, and $(11\bar{2}1)$ surfaces (top). The experimental SEM image is also included for comparison purposes. Energy profile connecting the ideal and experimental morphologies (bottom). E_{surf} in J m^{-2}.

Figure 10. Available morphologies of monoclinic $BiPO_4$ obtained by the Wulff construction considering the (010), (100), (101), (011), $(1\bar{1}2)$, (111), $(001,)$ and $(1\bar{1}0)$ surfaces (top). Experimental SEM images are also included for comparison purposes. Energy profile connecting the ideal and experimental morphologies (bottom). E_{surf} in J m^{-2}.

microscopy image of an individual $BiPO_4$ nanoparticle shows the presence of the $(10\bar{1}1)$ plane in the hexagonal phase.

In the case of the monoclinic phase of $BiPO_4$ [Figure 10 (top)], the ideal morphology is controlled by the (010), (100), (101), and (011) surfaces. The experimental morphology was simulated by means of two paths: the first from shape A and by stabilization of the $(1\bar{1}2)$ surface to obtain shape A1 and subsequently by stabilization of (100) and destabilization of (101) simultaneously, to obtain shape A2. The second path was reached by stabilization of the $(1\bar{1}0)$ surface, which is theoretically the most unstable surface, and (011) surface simultaneously to obtain shape B1 and destabilization of the (101) surface, to obtain shape B2. We have associated our

experimental morphologies with the B1 and B2 shapes. The A2 and D morphologies generated are similar to that reported by Li et al.[21]

Furthermore, the polyhedron energy (E_{poly}) was calculated, and also the energy profiles that allow one to connect the ideal morphology with the final experimental morphology were constructed and are depicted in Figures 9 and 10 (bottom) for the $BiPO_4$ hexagonal and monoclinic, respectively. The reaction diagram to obtain the final experimental morphologies of the $BiPO_4$ hexagonal evidences a less thermodynamically favorable process barrier [Figure 9 (bottom)], while the reaction path for the $BiPO_4$ monoclinic presents a minimum of energy via morphology B1 [Figure 10 (bottom)]. The

parameters used to calculate E_{poly} are reported in Tables SI-10 and SI-11.

According to Table SI-8 for hexagonal $BiPO_4$, there is a correlation between the surface stability and broken bond number (N_b). The $(10\bar{1}0)$ and (0001) surfaces have the lowest energy with similar values of E_{surf} = 0.44 and 0.47 J m^{-2}, respectively, and the lowest value of the broken bond number (N_b = 2), establishing an equal stability order for these two surfaces. The $(10\bar{1}1)$, $(11\bar{2}0)$, $(10\bar{1}2)$, $(11\bar{2}2)$, and $(11\bar{2}1)$ surfaces follow a decreasing order of stability with E_{surf} = 0.52, 0.55, 1.06, 1.28, and 1.39 J m^{-2}, respectively, and with N_b = 4, 6, 8, 12, and 14, respectively.

In the case of the monoclinic $BiPO_4$ (Table SI-9), the (010) and (100) surfaces have the lowest energy with similar values E_{surf} = 0.66 and 0.69 J m^{-2}, respectively, with the same broken bond number N_b = 2. The (101) and (011) surfaces with E_{surf} = 0.86 and 1.05 J m^{-2}, respectively, with an equal value of N_b = 4. Additionally, the $(1\bar{1}2)$, (111), (001), and $(1\bar{1}0)$ surfaces present decreasing order of stability from values E_{surf} = 1.23, 1.36, 1.74, and 2.56 J m^{-2}, respectively, with N_b = 6, 8, 12, and 14. Therefore, in this case, we are unable to establish a correlation between the surface stability and broken bond number.

In relation to the electronic properties of the surfaces (Figures SI-6B and SI-7B), in both the hexagonal and monoclinic phases, all surfaces present an insulating band gap as the original bulk. The energy-gap values for each surface are presented in Tables SI-8 and SI-9 for the hexagonal and monoclinic phases, respectively.

In general, on the surfaces of both polymorphs, the main contributors to the VB region are the O 2p and P 3p orbitals with fewer contributions from the Bi 3s orbitals. To the CB predominantly, we observed the Bi 3p and P 3p orbitals, on the $(10\bar{1}2)$ and (0001) surfaces of the hexagonal phase and the $(1\bar{1}0)$ and (111) surfaces of the monoclinic phase, where important contributions from the P 3p orbitals are observed. The presence of undercoordinated clusters on the surfaces modifies the distribution of the electron states and induces the formation of intermediate energy levels, flat bands in the band gap region. Thus, in the monoclinic phase, the band gap of the surfaces decreases as V_O increase, while in the hexagonal phase, the band gap is reduced on the $(10\bar{1}1)$, $(10\bar{1}2)$, and $(11\bar{2}1)$ surfaces because of the presence of an undercoordinated cluster of $[PO_3 \cdot V_O^x]$ and $[PO_2 \cdot 2V_O^x]$. V_O also split off in the O 2p orbitals in the VB region observed.

Photodegradation Process. The photocatalytic activity of the $BiPO_4$ samples was tested for chromophore degradation of RhB under visible-light irradiation. RhB shows a characteristic absorption peak located at 556 nm, relative to its conjugated chromophore xanthene ring, and in the presence of light and $BiPO_4$, it undergoes a hypochromic absorption displacement as a result of the deethylation of the N,N'-diethylammonium functional groups.[33] When the RhB solution was subjected to visible-light irradiation without a catalyst (photolysis test), practically no degradation was observed. The photodegradation results are shown in Figure 11A by variation of the RhB concentration (C_t/C_0) as a function of the irradiation time, with C_t and C_0 being the concentration at time t and the initial concentration, respectively. Because most of the heterogeneous photocatalytic mechanisms for semiconductors are considered to be pseudo-first-order reaction as a result of the low initial concentration of dye and the
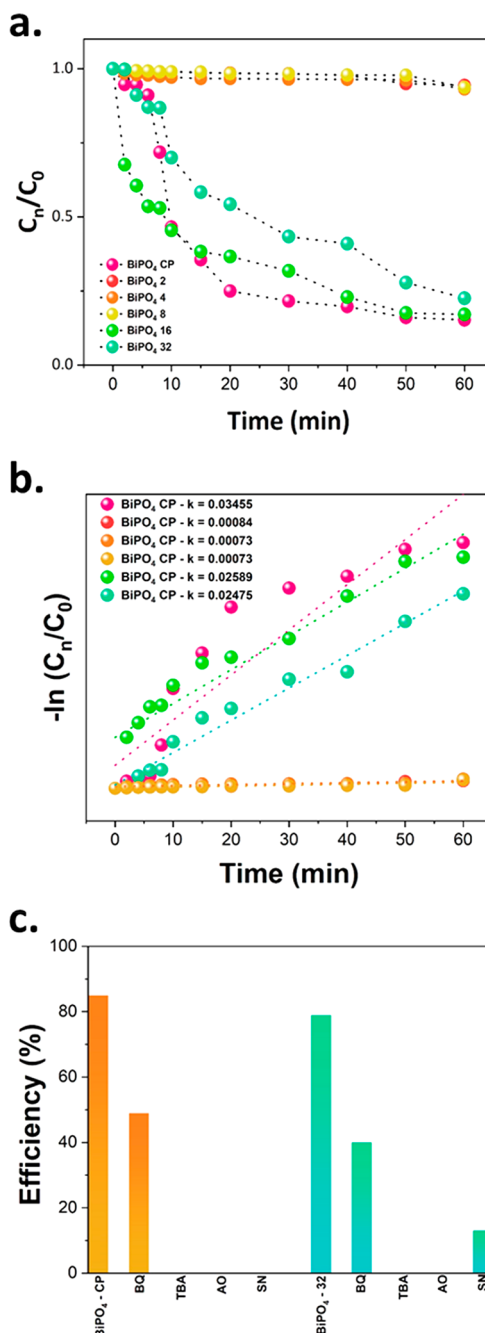

Figure 11. (a) Relative concentration of RhB dye (C_t/C_0). (b) Reaction kinetics of the RhB degradation $-\ln(C_t/C_0)$ versus time (min) for $BiPO_4$ powders. (c) Efficiency of degradation (%) of RhB dye under exposure to UV–vis radiation in the presence of different scavengers for $BiPO_4$ CP and irradiation by microwaves for 32 min.

constant concentration of catalyst, the Langmuir–Hinshelwood (L–H) model was used:[79,80]

$$\ln\left(\frac{C_t}{C_0}\right) = kt$$

(6)

Here k is the rate constant and t the reaction time. Therefore, if the reaction order is pseudo-first-order, the plot of $-\ln(C_t/C_0)$ as a function of the irradiation time gives a straight line in which the angular coefficient is the k value. The L–H plots were performed in order to verify the reaction order and to

obtain the rate constant for all samples, as shown in Figure 11B.

The photodegradation behavior change is observed according to the time employed at microwave irradiation. The hexagonal phase $BiPO_4$ synthesized by the CP method has an 85% rate of RhB chromophore photodegradation. After the sample was subjected to microwave irradiation for 2, 4, and 8 min, an inhibition of photodegradation activity was observed. This happens because the surfaces employed in the electron–hole recombination process of the hexagonal phase of $BiPO_4$ observed predominantly in these samples (2, 4, and 8 min) are different from that observed in the $BiPO_4$ sample obtained by the CP method. Surface stabilization of the obtained materials is intrinsically linked to the kinetic change in the balance of ordered and disordered $[BiO_6]$ clusters due to microwave action. The sample obtained by the CP method has no defined surfaces and may have several different types of V_O on its surface, coming from both Bi and P clusters. When the hexagonal samples of $BiPO_4$ obtained at 2, 4, and 8 min by microwave irradiation are analyzed, we can observe stabilization of the surfaces $(10\bar{1}0)$, which has two clusters with V_O ($[BiO_5 \cdot V_O^x]$), and $(11\bar{2}0)$, which has three V_O in the clusters $[BiO_5 \cdot V_O^x]$ and $[BiO_4 \cdot 2V_O^x]$. The stabilized surfaces employed in the photodegradation process cannot perform electron–hole recombination, becoming ineffective in this process. Moving from the hexagonal phase to the monoclinic phase of the $BiPO_4$, at the 16 and 32 min samples, efficiencies of 83 and 79% are observed for photodegradation, respectively. This is due to stabilization of the surfaces (011), which has two clusters with V_O ($[BiO_5 \cdot V_O^x]$), (101), which has two clusters with V_O ($[BiO_5 \cdot V_O^x]$), and $(1\bar{1}0)$, which has six V_O in the clusters $[BiO_5 \cdot V_O^x]$, $[BiO_4 \cdot 2V_O^x]$, and $[PO_2 \cdot 2V_O^x]$.

The photocatalytic activity is dependent on the electron–hole recombination rate of the material. The hexagonal structure of $BiPO_4$ obtained by the CP method has a high degree of order/disorder, so the electron–hole recombination rate is more effective, enabling RhB photodegradation. Analyzing the structures obtained in 2, 4, and 8 min, the hexagonal phase reorganization was observed, resulting in new morphologies of $BiPO_4$. The results obtained for these samples at long distance (XRD) correspond with an increase of material organization, creating new active sites and reducing electron–hole recombination. The transformation from hexagonal to monoclinic structure causes a structural reorganization, generating new active sites for electron–hole stabilization, making the photodegradation process of RhB effective again.

Because of these results, photocatalytic experiments using scavenger reagents were performed for the $BiPO_4$ CP and 32 min irradiation samples, in order to understand the photodegradation mechanism. As controls for these experiments, *tert*-butyl alcohol (TBA), silver nitrate (SN), *p*-benzoquinone (BQ), and ammonium oxalate (AO) were used as scavengers for hydroxyl radicals, electrons, superoxide radicals, and holes, respectively. Figure 11C shows the photodegradation efficiency of samples of $BiPO_4$ with and without scavengers. All of the experiments for both samples, i.e., the absence of hydroxyl radicals, electrons, superoxide radicals, and holes for reactions, presented inhibited or lower photodegradation efficiency compared to the $BiPO_4$ samples without scavengers. From these results, we propose a photodegradation mechanism, as given by Figure 12, which were constructed with Kröger–Vink notation.[81]
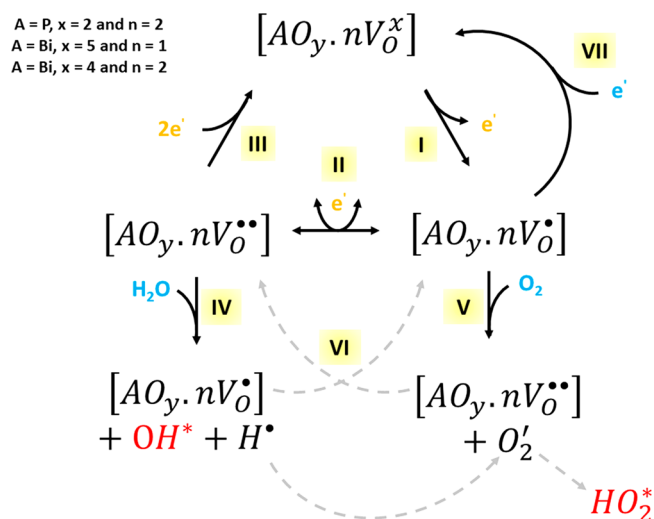

Figure 12. Mechanism for the generation of ROS of the $BiPO_4$ samples.

In Figure 12, the $BiPO_4$ surface clusters are represented for the general formula $[AO_y \cdot nV_O^x]$ (where A = P and Bi, $y = 2$, 4, and 5, and $n = 1$ and 2 to represent $[PO_2 \cdot 2V_O^x]$, $[BiO_4 \cdot 2V_O^x]$, and $[BiO_5 \cdot V_O^x]$). The V_O^x present in the clusters can become $V_O^{\bullet}$ and $V_O^{\bullet\bullet}$ according to the movement of electrons and holes in the $BiPO_4$ surface by cluster–cluster charge transfer (I–II in Figure 12). Losing electrons (I and II in Figure 12), the formation of $V_O^{\bullet}$ and $V_O^{\bullet\bullet}$ in the clusters favors the processes that lead to oxidation of H_2O and reduction of O_2 (IV and V in Figure 12), which generate reactive oxygen species (ROS), the hydroxyl radical OH*, and the hydroperoxyl radical HO_2^*. This process can be observed for samples obtained by the CP method and at 16 and 32 min of microwave irradiation. After ROS production, the clusters regenerate, continuing the oxidation processes (VI in Figure 12). HO_2^* is generated by the reaction of the proton ($H^{\bullet}$) with the superoxide radical O_2^{-}.[82] Electron recovery for the formation of V_O^x is not favorable for photocatalysis oxidation processes, which probably occur for samples obtained at 2, 4, and 8 min of microwave irradiation (III and VII in Figure 12).

■ CONCLUSIONS

As has emerged from this work, microwave irradiation upon materials can be exploited for the enhancement of phase transition. Here, we present a combined theoretical and experimental study dedicated to analysis of the microwave-driven hexagonal-to-monoclinic transition in $BiPO_4$. The study has been made possible by a combination of experimental techniques (XRD with Rietveld refinement, SEM, and micro-Raman and UV–vis spectroscopies, and PL measurements) and first-principles calculations at the DFT level. We have observed the phase transition of hexagonal to monoclinic $BiPO_4$ under microwave irradiation; in addition, by analysis of the structural electronic differences between these polymorphs and their exposed surfaces, the highest photocatalytic activity of monoclinic $BiPO_4$ exhibited upon comparison to hexagonal $BiPO_4$ is disclosed.

The main conclusions of this work can be summarized as follows:

(i) $BiPO_4$ crystals with hexagonal structure were successfully synthesized by a simple CP method, and for the first time, the effect the microwave irradiation to induce the irreversible

phase transition from hexagonal to monoclinic $BiPO_4$ polymorph has been reported. Hexagonal $BiPO_4$ is unstable under microwave irradiation, spontaneously transforming to the monoclinic phase $BiPO_4$ in short time and thus enhancing the photocatalytic performance of $BiPO_4$.

(ii) The first-principles calculations performed at the DFT level provide an in-depth understanding of the electronic and structural properties of the bulk and selected surfaces of both polymorphs of $BiPO_4$, namely, hexagonal and monoclinic.

(iii) A detailed analysis of the low vibrational modes of both hexagonal and monoclinic polymorphs shows that the movements associated with these modes are the key to explaining the irreversible phase transformation of hexagonal to monoclinic, which is induced by microwave irradiation.

(iv) The present understanding suggests that structural and electronic distortions of the $[PO_4]$ and $[BiO_6]$ clusters produced by microwave irradiation are capable of decreasing the energetic barrier of the path connecting the two polymorphs.

(v) On the basis of analysis of the geometry and electronic properties of the undercoordinated clusters (local coordination of the P and Bi cations) appearing at the exposed surfaces of the morphology, we are capable of rationalizing the mechanism of the photodegradation process of RhB under visible-light irradiation.

Our findings elucidate the structural and electronic alterations along the phase transition between the hexagonal and monoclinic phases of $BiPO_4$, which are induced by microwaves; further, these results serve as guidelines for engineers to optimize the structure and performance of future photocatalysts for environmental remediation applications.

■ ASSOCIATED CONTENT

ⓈI Supporting Information

The Supporting Information is available free of charge at https://pubs.acs.org/doi/10.1021/acs.inorgchem.0c00181.

> Rietveld refinements, PL spectra, lattice parameters, unit cell volume, and statistical parameters, Raman modes (cm^{-1}) compared to the literature, band structure, DOS and PDOS of the bulk and surfaces, calculated values of the surface energy, number of broken bonds, and polyhedron energy (PDF)

■ AUTHOR INFORMATION

Corresponding Author

Elson Longo − *Chemistry Department, CDMF, LIEC, Federal University of São Carlos, São Carlos, São Paulo 13565-905, Brazil;* ⓞ orcid.org/0000-0001-8062-7791; Email: elson.liec@gmail.com

Authors

Ana C. M. Tello − *Chemistry Department, CDMF, LIEC, Federal University of São Carlos, São Carlos, São Paulo 13565-905, Brazil; Instituto de Química de São Carlos, Universidade de São Paulo, São Carlos, São Paulo 13566-590, Brazil*

Marcelo Assis − *Chemistry Department, CDMF, LIEC, Federal University of São Carlos, São Carlos, São Paulo 13565-905, Brazil;* ⓞ orcid.org/0000-0003-0355-5565

Ricardo Menasce − *Chemistry Department, CDMF, LIEC, Federal University of São Carlos, São Carlos, São Paulo 13565-905, Brazil*

Amanda F. Gouveia − *Chemistry Department, CDMF, LIEC, Federal University of São Carlos, São Carlos, São Paulo 13565-905, Brazil;* ⓞ orcid.org/0000-0003-3441-3674

Vinicius Teodoro − *Chemistry Department, CDMF, LIEC, Federal University of São Carlos, São Carlos, São Paulo 13565-905, Brazil*

Natalia Jacomaci − *CDMF, LIEC, Chemistry Institute of the Paulista State University, UNESP, Araraquara, São Paulo 14801903, Brazil*

Maria A. Zaghete − *CDMF, LIEC, Chemistry Institute of the Paulista State University, UNESP, Araraquara, São Paulo 14801903, Brazil*

Juan Andrés − *Department of Physical and Analytical Chemistry, University Jaume I, Castelló 12071, Spain;* ⓞ orcid.org/0000-0003-0232-3957

Gilmar E. Marques − *Physics Department, Federal University of São Carlos, São Carlos, São Paulo 13565-905, Brazil*

Marcio D. Teodoro − *Physics Department, Federal University of São Carlos, São Carlos, São Paulo 13565-905, Brazil*

Albérico B. F. da Silva − *Instituto de Química de São Carlos, Universidade de São Paulo, São Carlos, São Paulo 13566-590, Brazil*

Jefferson Bettini − *Brazilian Nanotechnology National Laboratory, Campinas, São Paulo BR-13083100, Brazil*

Complete contact information is available at:
https://pubs.acs.org/10.1021/acs.inorgchem.0c00181

Author Contributions

The manuscript was written through contributions of all authors. All authors have given approval to the final version of the manuscript. These authors contributed equally.

Notes

The authors declare no competing financial interest.

■ ACKNOWLEDGMENTS

■ REFERENCES

(1) Pan, C.; Zhu, Y. New Type of $BiPO_4$ Oxy-Acid Salt Photocatalyst with High Photocatalytic Activity on Degradation of Dye. *Environ. Sci. Technol.* **2010**, *44*, 5570−5574.

(2) Lv, Y.; Zhu, Y.; Zhu, Y. Enhanced Photocatalytic Performance for the $BiPO_{4-x}$ Nanorod Induced by Surface Oxygen Vacancy. *J. Phys. Chem. C* **2013**, *117*, 18520−18528.

(3) Krause-Rehberg, R.; Leipner, H. S. *Positron Annihilation in Semiconductors: Defect Studies*; Springer Science & Business Media, 1999.

(4) Wang, H.; Yuan, X.; Wu, Y.; Zeng, G.; Tu, W.; Sheng, C.; Deng, Y.; Chen, F.; Chew, J. W. Plasmonic Bi Nanoparticles and BiOCl Sheets as Cocatalyst Deposited on Perovskite-Type $ZnSn(OH)_6$ Microparticle with Facet-Oriented Polyhedron for Improved Visible-Light-Driven Photocatalysis. *Appl. Catal., B* **2017**, *209*, 543−553.

(5) Fang, W.; Jiang, Z.; Yu, L.; Liu, H.; Shangguan, W.; Terashima, C.; Fujishima, A. Novel Dodecahedron BiVO$_4$:YVO$_4$ Solid Solution with Enhanced Charge Separation on Adjacent Exposed Facets for Highly Efficient Overall Water Splitting. *J. Catal.* 2017, 352, 155−159.

(6) Liu, Y.; Lv, Y.; Zhu, Y.; Liu, D.; Zong, R.; Zhu, Y. Fluorine Mediated Photocatalytic Activity of BiPO$_4$. *Appl. Catal., B* 2014, 147, 851−857.

(7) Li, J.; Dong, X.; Sun, Y.; Cen, W.; Dong, F. Facet-Dependent Interfacial Charge Separation and Transfer in Plasmonic Photocatalysts. *Appl. Catal., B* 2018, 226, 269−277.

(8) Wang, J.; Li, J.; Li, H.; Duan, S.; Meng, S.; Fu, X.; Chen, S. Crystal Phase-Controlled Synthesis of BiPO$_4$ and the Effect of Phase Structure on the Photocatalytic Degradation of Gaseous Benzene. *Chem. Eng. J.* 2017, 330, 433−441.

(9) Pan, C.; Li, D.; Ma, X.; Chen, Y.; Zhu, Y. Effects of Distortion of PO$_4$ Tetrahedron on the Photocatalytic Performances of BiPO$_4$. *Catal. Sci. Technol.* 2011, 1, 1399−1405.

(10) Achary, S. N.; Errandonea, D.; Muñoz, A.; Rodríguez-Hernández, P.; Manjón, F. J.; Krishna, P. S. R.; Patwe, S. J.; Grover, V.; Tyagi, A. K. Experimental and Theoretical Investigations on the Polymorphism and Metastability of BiPO$_4$. *Dalt. Trans.* 2013, 42 (42), 14999−15015.

(11) Liu, Y.-F.; Ma, X.-G.; Yi, X.; Zhu, Y.-F. Controllable Synthesis and Photocatalytic Performance of Bismuth Phosphate Nanorods. *Acta Physico-Chimica Sinica.* 2012, 28, 654−660.

(12) Xue, F.; Li, H.; Zhu, Y.; Xiong, S.; Zhang, X.; Wang, T.; Liang, X.; Qian, Y. Solvothermal Synthesis and Photoluminescence Properties of BiPO$_4$ Nano-Cocoons and Nanorods with Different Phases. *J. Solid State Chem.* 2009, 182, 1396−1400.

(13) Li, G.; Ding, Y.; Zhang, Y.; Lu, Z.; Sun, H.; Chen, R. Microwave Synthesis of BiPO$_4$ Nanostructures and Their Morphology-Dependent Photocatalytic Performances. *J. Colloid Interface Sci.* 2011, 363, 497−503.

(14) Geng, J.; Hou, W. H.; Lv, Y. N.; Zhu, J. J.; Chen, H. Y. One-Dimensional BiPO$_4$ Nanorods and Two-Dimensional BiOCl Lamellae: Fast Low-Temperature Sonochemical Synthesis, Characterization, and Growth Mechanism. *Inorg. Chem.* 2005, 44, 8503−8509.

(15) Pan, C.; Xu, J.; Wang, Y.; Li, D.; Zhu, Y. Dramatic Activity of C$_3$N$_4$/BiPO$_4$ Photocatalyst with Core/Shell Structure Formed by Self-Assembly. *Adv. Funct. Mater.* 2012, 22, 1518−1524.

(16) Guan, M.; Sun, J.; Tao, F.; Xu, Z. A Host Crystal for the Rare-Earth Ion Dopants: Synthesis of Pure and Ln-Doped Urchinlike BiPO$_4$ Structure and Its Photoluminescence. *Cryst. Growth Des.* 2008, 8, 2694−2697.

(17) Zhang, Q.; Tian, H.; Li, N.; Chen, M.; Teng, F. Controllable Growth of Novel BiPO$_4$ Dendrites by an Innovative Approach and High Energy Facets-Dependent Photocatalytic Activity. *CrystEngComm* 2014, 16, 8334−8339.

(18) Wu, Z.; Liu, J.; Tian, Q.; Wu, W. Efficient Visible Light Formaldehyde Oxidation with 2D P-n Heterostructure of BiOBr/BiPO$_4$ Nanosheets at Room Temperature. *ACS Sustainable Chem. Eng.* 2017, 5, 5008−5017.

(19) Lv, H.; Guang, J.; Liu, Y.; Tang, H.; Zhang, P.; Lu, Y.; Wang, J. Synthesis of Ionic Liquid-Modified BiPO$_4$ Microspheres with Hierarchical Flower-like Architectures and Enhanced Photocatalytic Activity. *RSC Adv.* 2015, 5, 100625−100632.

(20) Errandonea, D.; Gomis, O.; Santamaría-Perez, D.; García-Domene, B.; Muñoz, A.; Rodríguez-Hernández, P.; Achary, S. N.; Tyagi, A. K.; Popescu, C. Exploring the High-Pressure Behavior of the Three Known Polymorphs of BiPO$_4$: Discovery of a New Polymorph. *J. Appl. Phys.* 2015, 117, 105902.

(21) Li, P.; Yuan, T.; Li, F.; Zhang, Y. Phosphate Ion-Driven BiPO$_4$:Eu Phase Transition. *J. Phys. Chem. C* 2019, 123, 4424−4432.

(22) Naidu, B. S.; Vishwanadh, B.; Sudarsan, V.; Vatsa, R. K. BiPO$_4$: A Better Host for Doping Lanthanide Ions. *Dalt. Trans.* 2012, 41, 3194−3203.

(23) Ding, C.; Han, A.; Ye, M.; Zhang, Y.; Yao, L.; Yang, J. Hydrothermal Synthesis and Characterization of Novel Yellow

Pigments Based on V^{5+} Doped BiPO$_4$ with High Near-Infrared Reflectance. *RSC Adv.* 2018, 8, 19690−19700.

(24) Lv, Y.; Liu, Y.; Zhu, Y.; Zhu, Y. Surface Oxygen Vacancy Induced Photocatalytic Performance Enhancement of a BiPO$_4$ Nanorod. *J. Mater. Chem. A* 2014, 2, 1174−1182.

(25) Stuerga, D. Microwaves. In *Organic Synthesis*; Hoz, A. D. L. H., Loupy, A., Eds.; Wiley-VCH Verlag GmbH & Co. KGaA: Weinheim, Germany, 2012.

(26) Kappe, C. O.; Pieber, B.; Dallinger, D. Microwave Effects in Organic Synthesis: Myth or Reality? *Angew. Chem., Int. Ed.* 2013, 52, 1088−1094.

(27) Kappe, C. O. How to Measure Reaction Temperature in Microwave-Heated Transformations. *Chem. Soc. Rev.* 2013, 42, 4977−4990.

(28) Landry, C. C.; Lockwood, J.; Barron, A. R. Synthesis of Chalcopyrite Semiconductors and Their Solid Solutions by Microwave Irradiation. *Chem. Mater.* 1995, 7, 699−706.

(29) Komarneni, S.; Katsuki, H. Nanophase Materials by a Novel Microwave-Hydrothermal Process. *Pure Appl. Chem.* 2002, 74, 1537−1543.

(30) Macario, L. R.; Moreira, M. L.; Andrés, J.; Longo, E. An Efficient Microwave-Assisted Hydrothermal Synthesis of BaZrO$_3$ Microcrystals: Growth Mechanism and Photoluminescence Emissions. *CrystEngComm* 2010, 12, 3612−3619.

(31) Polshettiwar, V.; Varma, R. S. Green Chemistry by Nano-Catalysis. *Green Chem.* 2010, 12, 743−754.

(32) Bilecka, I.; Niederberger, M. Microwave Chemistry for Inorganic Nanomaterials Synthesis. *Nanoscale* 2010, 2, 1358−1374.

(33) Pereira, P. F. S.; Gouveia, A. F.; Assis, M.; de Oliveira, R. C.; Pinatti, I. M.; Penha, M.; Gonçalves, R. F.; Gracia, L.; Andrés, J.; Longo, E. ZnWO$_4$ Nanocrystals: Synthesis, Morphology, Photoluminescence and Photocatalytic Properties. *Phys. Chem. Chem. Phys.* 2018, 20, 1923−1937.

(34) Ebadi, M.; Mat-Teridi, M. A.; Sulaiman, M. Y.; Basirun, W. J.; Asim, N.; Ludin, N. A.; Ibrahim, M. A.; Sopian, K. Electrodeposited P-Type Co$_3$O$_4$ with High Photoelectrochemical Performance in Aqueous Medium. *RSC Adv.* 2015, 5, 36820−36827.

(35) Stuerga, D. Microwave-Material Interactions and Dielectric Properties, Key Ingredients for Mastery of Chemical Microwave Processes. Microwaves. In *Organic Synthesis*; Hoz, A. D. L. H., Loupy, A., Eds.; Wiley-VCH Verlag GmbH & Co. KGaA: Weinheim, Germany, 2016.

(36) Xu, Y.; Ma, X.; Hu, J.; Xu, A.; Wang, Z.; Huang, C. Structures and Energetics of Low-Index Stoichiometric BiPO$_4$ Surfaces. *CrystEngComm* 2019, 21, 4730−4739.

(37) Zheng, X.; Wang, J.; Liu, J.; Wang, Z.; Chen, S.; Fu, X. Photocatalytic Degradation of Benzene over Different Morphology BiPO$_4$: Revealing the Significant Contribution of High−Energy Facets and Oxygen Vacancies. *Appl. Catal., B* 2019, 243, 780−789.

(38) Lee, C.; Yang, W.; Parr, R. G. Development of the Colle-Salvetti Correlation-Energy Formula into a Functional of the Electron Density. *Phys. Rev. B: Condens. Matter Mater. Phys.* 1988, 37, 785−789.

(39) Dovesi, R.; Orlando, R.; Erba, A.; Zicovich-Wilson, C. M.; Civalleri, B.; Casassa, S.; Maschio, L.; Ferrabone, M.; De La Pierre, M.; D'Arco, P.; et al. CRYSTAL14: A Program for the Ab Initio Investigation of Crystalline Solids. *Int. J. Quantum Chem.* 2014, 114, 1287−1317.

(40) Heifets, E.; Kotomin, E. A.; Bagaturyants, A. A.; Maier, J. Ab Initio Study of BiFeO$_3$: Thermodynamic Stability Conditions. *J. Phys. Chem. Lett.* 2015, 6, 2847−2851.

(41) Peintinger, M. F.; Oliveira, D. V.; Bredow, T. Consistent Gaussian Basis Sets of Triple-Zeta Valence with Polarization Quality for Solid-State Calculations. *J. Comput. Chem.* 2013, 34, 451−459.

(42) Monkhorst, H. J.; Pack, J. D. Special Points for Brillouin-Zone Integrations. *Phys. Rev. B* 1976, 13, 5188−5192.

(43) Barmparis, G. D.; Lodziana, Z.; Lopez, N.; Remediakis, I. N. Nanoparticle Shapes by Using Wulff Constructions and First-Principles Calculations. *Beilstein J. Nanotechnol.* 2015, 6, 361−368.

(44) Wulff, G. XXV. Zur Frage der Geschwindigkeit des Wachsthums und der Auflösung der Krystallflächen. *Z. Kristallogr. - Cryst. Mater.* **1901**, *34*, 449−530.

(45) Andrés, J.; Gracia, L.; Gouveia, A. F.; Ferrer, M. M.; Longo, E. Effects of Surface Stability on the Morphological Transformation of Metals and Metal Oxides as Investigated by First-Principles Calculations. *Nanotechnology* **2015**, *26*, 405703.

(46) Fabbro, M. T.; Saliby, C.; Rios, L. R.; La Porta, F. A.; Gracia, L.; Li, M. S.; Andrés, J.; Santos, L. P. S.; Longo, E. Identifying and Rationalizing the Morphological, Structural, and Optical Properties of β-Ag$_2$MoO$_4$ Microcrystals, and the Formation Process of Ag Nanoparticles on Their Surfaces: Combining Experimental Data and First-Principles Calculations. *Sci. Technol. Adv. Mater.* **2015**, *16*, 065002.

(47) Bomio, M. R. D.; Tranquilin, R. L.; Motta, F. V.; Paskocimas, C. A.; Nascimento, R. M.; Gracia, L.; Andres, J.; Longo, E. Toward Understanding the Photocatalytic Activity of PbMoO$_4$ Powders with Predominant (111), (100), (011), and (110) Facets. A Combined Experimental and Theoretical Study. *J. Phys. Chem. C* **2013**, *117*, 21382−21395.

(48) Lu, J. J.; Ulrich, J. The Influence of Supersaturation on Crystal Morphology − Experimental and Theoretical Study. *Cryst. Res. Technol.* **2005**, *40*, 839−846.

(49) Longo, V. M.; Gracia, L.; Stroppa, D. G.; Cavalcante, L. S.; Orlandi, M.; Ramirez, A. J.; Leite, E. R.; Andrés, J.; Beltrán, A.; Varela, J. A.; et al. A Joint Experimental and Theoretical Study on the Nanomorphology of CaWO$_4$ Crystals. *J. Phys. Chem. C* **2011**, *115*, 20113−20119.

(50) Botelho, G.; Andres, J.; Gracia, L.; Matos, L. S.; Longo, E. Photoluminescence and Photocatalytic Properties of Ag$_3$PO$_4$ Microcrystals: An Experimental and Theoretical Investigation. *ChemPlusChem* **2016**, *81*, 202−212.

(51) Oliveira, M. C.; Gracia, L.; Nogueira, I. C.; Carmo Gurgel, M. F. do; Mercury, J. M. R.; Longo, E.; Andrés, J. Synthesis and Morphological Transformation of BaWO$_4$ Crystals: Experimental and Theoretical Insights. *Ceram. Int.* **2016**, *42*, 10913−10921.

(52) Silva, G. S.; Gracia, L.; Fabbro, M. T.; Serejo dos Santos, L. P.; Beltrán-Mir, H.; Cordoncillo, E.; Longo, E.; Andrés, J. Theoretical and Experimental Insight on Ag2CrO4Microcrystals: Synthesis, Characterization, and Photoluminescence Properties. *Inorg. Chem.* **2016**, *55* (17), 8961−8970.

(53) Gouveia, A. F.; Ferrer, M. M.; Sambrano, J. R.; Andrés, J.; Longo, E. Modeling the Atomic-Scale Structure, Stability, and Morphological Transformations in the Tetragonal Phase of LaVO$_4$. *Chem. Phys. Lett.* **2016**, *660*, 87−92.

(54) Gao, Z.; Sun, W.; Hu, Y.; Liu, X. Anisotropic Surface Broken Bond Properties and Wettability of Calcite and Fluorite Crystals. *Trans. Nonferrous Met. Soc. China* **2012**, *22*, 1203−1208.

(55) Gao, Z.; Fan, R.; Ralston, J.; Sun, W.; Hu, Y. Surface Broken Bonds: An Efficient Way to Assess the Surface Behaviour of Fluorite. *Miner. Eng.* **2019**, *130*, 15−23.

(56) Ferrer, M. M.; Gouveia, A. F.; Gracia, L.; Longo, E.; Andrés, J. A 3D Platform for the Morphology Modulation of Materials: First Principles Calculations on the Thermodynamic Stability and Surface Structure of Metal Oxides: Co$_3$O$_4$, α-Fe$_2$O$_3$, and In$_2$O$_3$. *Modell. Simul. Mater. Sci. Eng.* **2016**, *24*, 025007.

(57) Macedo, N. G.; Gouveia, A. F.; Roca, R. A.; Assis, M.; Gracia, L.; Andrés, J.; Leite, E. R.; Longo, E. Surfactant-Mediated Morphology and Photocatalytic Activity of α-Ag$_2$WO$_4$ Material. *J. Phys. Chem. C* **2018**, *122*, 8667−8679.

(58) Romero, B.; Bruque, S.; Aranda, M. A. G.; Iglesias, J. E. Syntheses, Crystal Structures, and Characterization of Bismuth Phosphates. *Inorg. Chem.* **1994**, *33*, 1869−1874.

(59) Zhu, L.; Ma, X.-G.; Wei, Y.; Chu, L.; Wang, H.-H.; Huang, C.-Y. Origin of Photocatalytic Activity of BiPO$_4$: The First-Principles Calculations. *Jiegou Huaxue* **2017**, *36*, 1299−1306.

(60) Darkwah, W. K.; Adormaa, B. B.; Christelle Sandrine, M. K.; Ao, Y. Modification Strategies for Enhancing the Visible Light

Responsive Photocatalytic Activity of the BiPO$_4$ Nano-Based Composite Photocatalysts. *Catal. Sci. Technol.* **2019**, *9*, 546−566.

(61) Gao, H.; Zheng, C.; Yang, H.; Niu, X.; Wang, S. Construction of a CQDs/Ag$_3$PO$_4$/BiPO$_4$ Heterostructure Photocatalyst with Enhanced Photocatalytic Degradation of Rhodamine B under Simulated Solar Irradiation. *Micromachines* **2019**, *10*, 557.

(62) Aguilar-Reynosa, A.; Romaní, A.; Ma. Rodríguez-Jasso, R.; Aguilar, C. N.; Garrote, G.; Ruiz, H. A. Microwave Heating Processing as Alternative of Pretreatment in Second-Generation Biorefinery: An Overview. *Energy Convers. Manage.* **2017**, *136*, 50−65.

(63) Errandonea, D.; Gomis, O.; Rodriguez-Hernández, P.; Muñoz, A.; Ruiz-Fuertes, J.; Gupta, M.; Achary, S. N.; Hirsch, A.; Manjon, F. J.; Peters, L.; et al. High-Pressure Structural and Vibrational Properties of Monazite-Type BiPO$_4$, LaPO$_4$, CePO$_4$, and PrPO$_4$. *J. Phys.: Condens. Matter* **2018**, *30*, 65401.

(64) Lakshminarayana, G.; Dao, T. D.; Chen, K.; Sharma, M.; Takeda, T.; Brik, M. G.; Kityk, I. V.; Singh, S.; Nagao, T. Effect of Different Surfactants on Structural and Optical Properties of Ce^{3+} and Tb^{3+} Co-Doped BiPO$_4$ Nanostructures. *Opt. Mater. (Amsterdam, Neth.)* **2015**, *39*, 110−117.

(65) Li, J.; Yuan, H.; Zhu, Z. First-Principles Energy Band Calculation and One Step Synthesis of N-Doped BiPO$_4$. *J. Alloys Compd.* **2015**, *640*, 290−297.

(66) Pan, C.; Zhu, Y. A Review of BiPO4{,} a Highly Efficient Oxyacid-Type Photocatalyst{,} Used for Environmental Applications. *Catal. Sci. Technol.* **2015**, *5* (6), 3071−3083.

(67) Milanez, J.; de Figueiredo, A. T.; de Lazaro, S.; Longo, V. M.; Erlo, R.; Mastelaro, V. R.; Franco, R. W. A.; Longo, E.; Varela, J. A. The Role of Oxygen Vacancy in the Photoluminescence Property at Room Temperature of the CaTiO$_3$. *J. Appl. Phys.* **2009**, *106* (4), 043526.

(68) Longo, V. M.; Cavalcante, L. S.; de Figueiredo, A. T.; Santos, L. P. S.; Longo, E.; Varela, J. A.; Sambrano, J. R.; Paskocimas, C. A.; De Vicente, F. S.; Hernandes, A. C. Highly Intense Violet-Blue Light Emission at Room Temperature in Structurally Disordered SrZrO$_3$ Powders. *Appl. Phys. Lett.* **2007**, *90*, 091906.

(69) Gracia, L.; Longo, V. M.; Cavalcante, L. S.; Beltrán, A.; Avansi, W.; Li, M. S.; Mastelaro, V. R.; Varela, J. A.; Longo, E.; Andrés, J. Presence of Excited Electronic State in CaWO$_4$ Crystals Provoked by a Tetrahedral Distortion: An Experimental and Theoretical Investigation. *J. Appl. Phys.* **2011**, *110*, 043501.

(70) Anicete-Santos, M.; Orhan, E.; de Maurera, M. A.; Simões, L. G. P.; Souza, A. G.; Pizani, P. S.; Leite, E. R.; Varela, J. A.; Andrés, J.; Beltrán, A.; et al. Contribution of Structural Order-Disorder to the Green Photoluminescence of PbWO$_4$. *Phys. Rev. B: Condens. Matter Mater. Phys.* **2007**, *75*, 165105.

(71) Stearns, E. I. Commission Internationale de L'Éclairage, Colorimetry. *Color Res. Appl.*, 2nd ed.; Publication CIE No. 15.2, 78; Central Bureau of the CIE: Gaithersburg, MD, 1987; Vol. *13*, pp 64 and 65.

(72) Tongay, S.; Suh, J.; Ataca, C.; Fan, W.; Luce, A.; Kang, J. S.; Liu, J.; Ko, C.; Raghunathanan, R.; Zhou, J.; et al. Defects Activated Photoluminescence in Two-Dimensional Semiconductors: Interplay between Bound, Charged, and Free Excitons. *Sci. Rep.* **2013**, *3*, 2657.

(73) Gupta, S. K.; Sudarshan, K.; Ghosh, P. S.; Srivastava, A. P.; Bevara, S.; Pujari, P. K.; Kadam, R. M. Role of Various Defects in the Photoluminescence Characteristics of Nanocrystalline Nd$_2$Zr$_2$O$_7$: An Investigation through Spectroscopic and DFT Calculations. *J. Mater. Chem. C* **2016**, *4*, 4988−5000.

(74) Wu, Z.; Zhao, W.; Jiang, J.; Zheng, T.; You, Y.; Lu, J.; Ni, Z. Defect Activated Photoluminescence in WSe$_2$ Monolayer. *J. Phys. Chem. C* **2017**, *121*, 12294−12299.

(75) Longo, V. M.; de Figueiredo, A. T.; de Lázaro, S.; Gurgel, M. F.; Costa, M. G. S.; Paiva-Santos, C. O.; Varela, J. A.; Longo, E.; Mastelaro, V. R.; DE Vicente, F. S.; et al. Structural Conditions That Leads to Photoluminescence Emission in SrTiO$_3$: An Experimental and Theoretical Approach. *J. Appl. Phys.* **2008**, *104*, 023515.

(76) Silva Junior, E.; La Porta, F. A.; Liu, M. S.; Andrés, J.; Varela, J. A.; Longo, E. A Relationship between Structural and Electronic

Order−Disorder Effects and Optical Properties in Crystalline TiO_2 Nanomaterials. *Dalt. Trans.* **2015**, *44*, 3159−3175.

(77) Klein, P. B.; Nwagwu, U.; Edgar, J. H.; Freitas, J. A. Photoluminescence Investigation of the Indirect Band Gap and Shallow Impurities in Icosahedral $B_{12}As_2$. *J. Appl. Phys.* **2012**, *112*, 013508.

(78) Hizhnyi, Y. A.; Nedilko, S. G.; Chornii, V. P.; Slobodyanik, M. S.; Zatovsky, I. V.; Terebilenko, K. V. Electronic Structures and Origin of Intrinsic Luminescence in Bi-Containing Oxide Crystals $BiPO_4$, $K_3Bi_5(PO_4)_6$, $K_2Bi(PO_4)(MoO_4)$, $K_2Bi(PO_4)(WO_4)$ and $K_5Bi(MoO_4)_4$. *J. Alloys Compd.* **2014**, *614*, 420−435.

(79) Liu, B.; Zhao, X.; Terashima, C.; Fujishima, A.; Nakata, K. Thermodynamic and Kinetic Analysis of Heterogeneous Photocatalysis for Semiconductor Systems. *Phys. Chem. Chem. Phys.* **2014**, *16*, 8751−8760.

(80) Kumar, K. V.; Porkodi, K.; Rocha, F. Langmuir−Hinshelwood Kinetics − A Theoretical Study. *Catal. Commun.* **2008**, *9*, 82−84.

(81) Kröger, F. A.; Vink, H. J. Relations between the Concentrations of Imperfections in Solids. *J. Phys. Chem. Solids* **1958**, *5*, 208−223.

(82) Trench, A. B.; Machado, T.; Gouveia, A. F.; Assis, M.; da Trindade, L. G.; Santos, C.; Perrin, A.; Perrin, C.; Oliva, M.; Andres, J.; Longo, E. Connecting Structural, Optical, and Electronic Properties and Photocatalytic Activity of Ag_3PO4:Mo Complemented by DFT Calculations. *Appl. Catal., B* **2018**, *238*, 198−211.